

We have presented the Graphical Abstract text and image for your article below. This brief summary of your work will appear in the contents pages of the issue in which your article appears.

PAPER

1

Strongly enhanced visible light photoelectrocatalytic hydrogen evolution reaction in an n-doped MoS₂/TiO₂(B) heterojunction by selective decoration of platinum nanoparticles at the MoS₂ edge sites

Kamal Kumar Paul, N. Sreekanth, Ravi K. Biroju, Alexander J. Pattison, Daniel Escalera-López, Anku Guha, Tharangattu N. Narayanan, Neil Vaughan Rees, Wolfgang Theis and P. K. Giri*

Herein, we demonstrate strongly enhanced visible light photoelectrocatalytic hydrogen evolution reaction (HER) in few-layer MoS₂ grown on a mesoporous TiO₂(B) nanobelt (NB) by selective decoration of platinum (Pt) nanoparticles (NPs) on the edge/defect sites of the MoS₂ layer.

Please check this proof carefully. Our staff will not read it in detail after you have returned it.

Please send your corrections either as a copy of the proof PDF with electronic notes attached or as a list of corrections. **Do not edit the text within the PDF or send a revised manuscript** as we will not be able to apply your corrections. Corrections at this stage should be minor and not involve extensive changes.

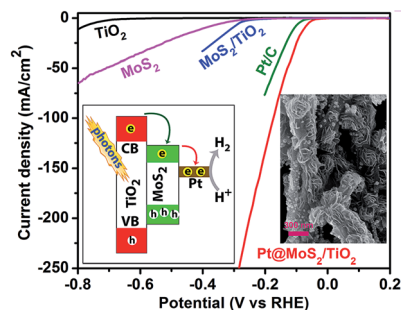
Proof corrections must be returned as a single set of corrections, approved by all co-authors. No further corrections can be made after you have submitted your proof corrections as we will publish your article online as soon as possible after they are received.

Please ensure that:

- The spelling and format of all author names and affiliations are checked carefully. You can check how we have identified the authors' first and last names in the researcher information table on the next page. **Names will be indexed and cited as shown on the proof, so these must be correct.**
- Any funding bodies have been acknowledged appropriately and included both in the paper and in the funder information table on the next page.
- All of the editor's queries are answered.
- Any necessary attachments, such as updated images or ESI files, are provided.

Translation errors can occur during conversion to typesetting systems so you need to read the whole proof. In particular please check tables, equations, numerical data, figures and graphics, and references carefully.

Please return your **final** corrections, where possible within **48 hours** of receipt, by e-mail to: materialsA@rsc.org. If you require more time, please notify us by email.



Funding information

Providing accurate funding information will enable us to help you comply with your funders' reporting mandates. Clear acknowledgement of funder support is an important consideration in funding evaluation and can increase your chances of securing funding in the future.

We work closely with Crossref to make your research discoverable through the Funding Data search tool (<http://search.crossref.org/funding>). Funding Data provides a reliable way to track the impact of the work that funders support. Accurate funder information will also help us (i) identify articles that are mandated to be deposited in **PubMed Central (PMC)** and deposit these on your behalf, and (ii) identify articles funded as part of the **CHORUS** initiative and display the Accepted Manuscript on our web site after an embargo period of 12 months.

Further information can be found on our webpage (<http://rsc.li/funding-info>).

What we do with funding information

We have combined the information you gave us on submission with the information in your acknowledgements. This will help ensure the funding information is as complete as possible and matches funders listed in the Crossref Funder Registry.

If a funding organisation you included in your acknowledgements or on submission of your article is not currently listed in the registry it will not appear in the table on this page. We can only deposit data if funders are already listed in the Crossref Funder Registry, but we will pass all funding information on to Crossref so that additional funders can be included in future.

Please check your funding information

The table below contains the information we will share with Crossref so that your article can be found *via* the Funding Data search tool. **Please check that the funder names and grant numbers in the table are correct and indicate if any changes are necessary to the Acknowledgements text.**

Funder name	Funder's main country of origin	Funder ID (for RSC use only)	Award/grant number
Ministry of Electronics and Information technology	India	501100008628	5(9)/2012-NANO(VOL-II)
Engineering and Physical Sciences Research Council	United Kingdom	501100000266	EP/G037116/1, EP/L015749/1; EP/N509590/1
Science and Engineering Research Board	India	501100001843	PDF/2016/002763

Researcher information

Please check that the researcher information in the table below is correct, including the spelling and formatting of all author names, and that the authors' first, middle and last names have been correctly identified. **Names will be indexed and cited as shown on the proof, so these must be correct.**

If any authors have ORCID or ResearcherID details that are not listed below, please provide these with your proof corrections. Please ensure that the ORCID and ResearcherID details listed below have been assigned to the correct author. Authors should have their own unique ORCID iD and should not use another researcher's, as errors will delay publication.

Please also update your account on our online [manuscript submission system](#) to add your ORCID details, which will then be automatically included in all future submissions. See [here](#) for step-by-step instructions and more information on author identifiers.

First (given) and middle name(s)	Last (family) name(s)	ResearcherID	ORCID iD
Kamal Kumar	Paul		
N.	Sreekanth	T-1162-2018	
Ravi K.	Biroju		

Alexander J.	Pattison		
Daniel	Escalera-López		
Anku	Guha		
Tharangattu N.	Narayanan		0000-0002-5201-7539
Neil Vaughan	Rees		
Wolfgang	Theis		
P. K.	Giri		0000-0003-2020-4249

Queries for the attention of the authors

Journal: **Journal of Materials Chemistry A**

Paper: **c8ta06783j**

Title: **Strongly enhanced visible light photoelectrocatalytic hydrogen evolution reaction in an n-doped MoS₂/TiO₂(B) heterojunction by selective decoration of platinum nanoparticles at the MoS₂ edge sites**

For your information: You can cite this article before you receive notification of the page numbers by using the following format: (authors), J. Mater. Chem. A, (year), DOI: 10.1039/c8ta06783j.

Editor's queries are marked on your proof like this **1**, **2**, etc. and for your convenience line numbers are indicated like this 5, 10, 15, ...

Please ensure that all queries are answered when returning your proof corrections so that publication of your article is not delayed.

Query Reference	Query	Remarks
1	Funder details have been incorporated in the funder table using information provided in the article text. Please check that the funder information in the table is correct.	
2	Please confirm that the spelling and format of all author names is correct. Names will be indexed and cited as shown on the proof, so these must be correct. No late corrections can be made.	
3	In the sentence beginning "Zhou <i>et al.</i> ³⁸ and..." should "employed" be changed to "decorated"?	
4	The sentence beginning "The weight% of..." has been altered for clarity. Please check that the meaning is correct.	
5	Please note that a conflict of interest statement is required for all manuscripts. Please read our policy on Conflicts of interest (http://rsc.li/conflicts) and provide a statement with your proof corrections. If no conflicts exist, please state that "There are no conflicts to declare".	
6	Ref. 31: Please provide the last name for the 1st author.	
7	Please check that the Graphical Abstract text fits within the allocated space indicated on the front page of the proof. If the entry does not fit between the two horizontal lines, then please trim the text and/or the title.	

Strongly enhanced visible light photoelectrocatalytic hydrogen evolution reaction in an n-doped MoS₂/TiO₂(B) heterojunction by selective decoration of platinum nanoparticles at the MoS₂ edge sites†

Cite this: DOI: 10.1039/c8ta06783j

Kamal Kumar Paul,^a N. Sreekanth,^b Ravi K. Biroju,^c Alexander J. Pattison,^c Daniel Escalera-López,^{cd} Anku Guha,^b Tharangattu N. Narayanan,^{ib} Neil Vaughan Rees,^d Wolfgang Theis^c and P. K. Giri^{ib*ae}

Herein, we demonstrate strongly enhanced visible light photoelectrocatalytic hydrogen evolution reaction (HER) in few-layer MoS₂ grown on a mesoporous TiO₂(B) nanobelt (NB) by selective decoration of platinum (Pt) nanoparticles (NPs) on the edge/defect sites of the MoS₂ layer. Three catalytically active components are anchored together to increase the photoelectrocatalytic HER activity synergistically, beyond that of commercial Pt/C electrodes (20 wt% Pt). An extremely low concentration of Pt NPs (1.4 wt%) with average size ~3.8 nm was decorated over the preferentially edge-site-exposed few-layer MoS₂, with lateral sizes 130–350 nm, as evidenced from high-angle annular dark-field STEM imaging. During the heterojunction formation, S is doped in the TiO₂ layer causing a high density of electrons in TiO₂ that migrate to the MoS₂ layer inducing n-type doping in it and thus TiO₂ acts as an efficient photocathode in photoelectrocatalysis. Quantitative XPS analysis reveals that the catalytically active bridging S₂²⁻/apical S²⁻ increases up to ~72% after the formation of the ternary system Pt@MoS₂/TiO₂(B). S-enriched MoS₂/TiO₂(B) selectively loaded with Pt NPs on the edge sites of MoS₂ exhibits a giant enhancement in the HER activity in an acidic medium under light. We record a nearly 16 fold higher exchange current density (0.296 mA cm⁻²) for the ternary system as compared to that of the MoS₂/TiO₂ binary system under visible light excitation. The marginally Pt loaded ternary system exhibits an extremely low charge transfer resistance (14 Ω) and a low overpotential as well as Tafel slope (–74 mV and 30 mV dec⁻¹, respectively) boosting the overall HER performance under visible light. Chronopotentiometric measurements reveal the high stability of binary and ternary systems to sustain a 10 mA cm⁻² cathodic current up to 12 hours. The results show that the marginally loaded Pt NPs activate the inert basal plane, edge sites of MoS₂ and porous sites of TiO₂, forming an integrated network where the photogenerated electrons can easily be injected from the TiO₂ to MoS₂ and then to Pt NPs, presenting a feasible approach to boost the HER activity under visible light.

Received 13th July 2018
Accepted 9th October 2018

DOI: 10.1039/c8ta06783j

rsc.li/materials-a

1. Introduction

The fast-rising energy crisis and environmental pollution are driving the development of new, sustainable, pollution-free sources that can be used on an industrial scale. Hydrogen is believed to be one of the most promising alternatives to fossil fuels and a source of renewable green energy due to its high energy density and carbon-free combustion emission. Solar-light-driven electrocatalysis using semiconductor TiO₂ and its heterostructures (HSs) is one of the most promising sustainable technologies for the generation of hydrogen by water splitting.^{1–7} To make the system commercially viable, the electrocatalyst should be solar light active, efficient and highly stable. To broaden the light harvesting window from UV to visible/NIR

^aDepartment of Physics, Indian Institute of Technology Guwahati, Guwahati-781039, India. E-mail: giri@iitg.ernet.in

^bTata Institute of Fundamental Research, Sy. No. 36/P, Gopanpally Village, Serilingampally Mandal, Ranga Reddy District, Hyderabad-500 107, India

^cNanoscale Physics Research Laboratory, School of Physics and Astronomy, University of Birmingham, Birmingham B15 2TT, UK

^dCentre for Hydrogen and Fuel Cell Research, School of Chemical Engineering, University of Birmingham, Edgbaston B15 2TT, Birmingham, UK

^eCentre for Nanotechnology, Indian Institute of Technology Guwahati, Guwahati-781039, India

† Electronic supplementary information (ESI) available. See DOI: 10.1039/c8ta06783j

and increase the catalytic activity, numerous strategies have been explored, including impurity doping,^{8–11} staggered-type HSs,^{12,13} TiO₂-based plasmonic HSs with noble metal nanoparticles (NPs),^{14–18} *etc.* In a heterostructured system, the presence of a heterojunction modifies the band positions as well as the inclination at the interface facilitating the migration of photogenerated charge carriers through the heterojunctions, which makes a highly efficient electrocatalyst.¹⁹ Though platinum (Pt) group noble metals are the most efficient conventional electrocatalysts, their extremely high cost and scarcity in nature hinder their industrial-scale usage.²⁰ Graphene-based two-dimensional (2D) transition metal dichalcogenide nanosheets, especially MoS₂ based heterostructures, have recently received much attention as a noble-metal-free catalyst and an anode material for energy storage devices.^{21–26} Recently, Pi *et al.*²⁷ demonstrated an extraordinary catalytic performance by TiO₂ nanostructures decorated with 1T-MoS₂ nanosheets under solar light. Thus, MoS₂ has now been recognized as an efficient co-catalyst incorporated with TiO₂ nanostructures due to its structural anisotropy, chemical inertness, good electroconductivity, and efficient catalytic properties.^{28–30} Theoretical and experimental studies found that the HER ability of MoS₂ mainly derives from the edge sites of its 2D layers, whereas the basal planes are catalytically inert, limiting its overall performance.³¹ Thus, tuning the architecture of MoS₂ to preferentially edge-exposed sites, semiconducting (2H) to metallic (1T) phase transformation, introduction of vacancies and incorporation with metal NPs are the synergistic strategies for the enhancement of HER activity.^{32–35} Recently, edge-site-activated ultra-thin MoS₂ nanostructures with optimum defect density, especially S-vacancies, have been identified as tunable active sites to stimulate the originally inert basal plane for the HER.^{36,37} Although these edge sites and defects in the MoS₂ lattice may introduce additional active sites on its basal plane, their incorporation hampers the electron transport properties, leading to low overall HER activity. Zhou *et al.*³⁸ and Li *et al.*²⁸ have modified the morphology of TiO₂ from ultra-small spherical NPs to long nanobelts (NBs) and employed few-layer MoS₂ nanosheets on them with high catalytic surface areas, which in turn enhanced the hydrogen generation efficiency synergistically. A few groups considered conductive carbon fiber cloths to decorate vertically aligned and preferentially edge-site-exposed MoS₂ nanostructures, which provide very low catalyst-electrode contact resistance, leading to enhanced HER performance.^{39,40} More recently, Xu *et al.*⁴ demonstrated a smart strategy of utilizing the inert basal plane by loading 2.45 wt% of Pt NPs on the porous MoS₂ nanostructures anchored vertically with the carbon fiber cloths. It was shown that the loaded Pt NPs could both serve as additional active HER sites and enable fast electron transport, which in turn reduce Pt consumption without compromising the HER activity. It may be noted that though there are several reports on the catalytic activity of binary MoS₂/Pt and TiO₂/Pt system, there is hardly any report on the TiO₂/MoS₂/Pt composite system.^{4,41–43} Very recently, photocatalytic and electrocatalytic H₂ generation in a TiO₂/Pt/MoS₂ composite system was reported by Li *et al.*⁴⁴ However, the system was not well characterized and the performance of the composite system was

comparable or inferior to that of binary systems. Unlike the earlier reports, we have chosen a porous TiO₂(B) nanobelt as a novel platform for the growth of edge site exposed few-layer MoS₂. Subsequently, Pt NPs are preferentially decorated at the edge sites of MoS₂ and porous sites of TiO₂(B) with ultralow concentration. To the best of our knowledge, a thorough understanding of such a ternary system and its visible light PEC activity has not been explored in the literature. In particular, the role of individual components in a ternary system needs to be addressed to exploit its application in next-generation photoelectrocatalysis experiments.

Herein, we carried out controlled growth of porous TiO₂(B) NBs (TB) *via* a solvothermal method and its *in situ* surface decoration with discrete few-layer MoS₂ by a second stage hydrothermal treatment. Incorporation of a marginal amount of Pt NPs as a suitable co-catalyst on the surface of MoS₂/TiO₂(B) (MSTB) can generate additional surface active sites, increasing the overall conductivity and charge separation through the multiple heterojunctions. The ternary catalyst contains the maximum amount of bridging S₂²⁻/apical S²⁻ which are known to be catalytically active. As the Pt NPs are decorated on the edge/porous sites of the MoS₂/TiO₂ (PMSTB) HS, the photoexcited electrons can easily be transferred from TiO₂ to Pt sites directly as well as *via* the MoS₂ edge-sites, leading to a remarkable enhancement in the exchange current density (*j*₀) and thus HER activity compared to that under dark conditions that is much higher than those of the pristine or the other HSs. Thus, a rational design of hierarchical nanostructures with a marginal amount of Pt loading (1.4 wt%) is crucial for achieving superior photoelectrocatalytic systems.

2. Experimental procedure

2.1. Preparation of TiO₂ NBs

Anatase TiO₂ nanopowder, ethylene glycol, and sodium hydroxide (NaOH) pellets were used in our experiments as received from Merck without any further purification. In a typical synthesis, 0.2 g of anatase TiO₂ powder (average particle size ~ 80 nm) was mixed vigorously in a 50 ml aqueous NaOH solution (10 M) with an equal volume of ethylene glycol. Next, the mixed white solution was transferred into a Teflon-lined autoclave (Berghof, BR-100) and the solution temperature was maintained at 220 °C monitored with a thermocouple inserted into the Teflon chamber for 16 h with constant magnetic stirring at 500 rpm. The resultant precipitates were washed thoroughly with DI water and 0.1 N HCl to reduce its pH to 7, which ensures the full exchange of Na⁺ with H⁺ ions. Then, the obtained H-titanate NBs were calcined at 500 °C for 5 h in air to get porous TiO₂(B) NBs.

2.2. Growth of MoS₂/TiO₂ NB heterostructures

Typically, 20 mg of TiO₂(B) NBs powder was homogeneously dispersed in 40 ml of Milli-Q water in bath sonication for 30 min. Next, 60 mg sodium molybdate (Na₂MoO₄·2H₂O) and 120 mg thioacetamide (C₂H₅NS) as a source of Mo and S, respectively were dissolved in the above dispersion.⁴⁵ The

mixture was then treated in a Teflon-lined stainless steel autoclave at 240 °C for 24 h with constant magnetic stirring at 250 rpm. The resultant black precipitate was washed thoroughly with DI water to eliminate the additional salts and impurities followed by centrifugation. Uniform decoration of few-layer MoS₂ on the TiO₂ NB platform with a 1 : 1 weight ratio of MoS₂ and TiO₂ was obtained after a drying process at 50 °C for 12 h. For comparison, pure few-layer MoS₂ was synthesized under identical conditions but in the absence of a TiO₂ NB platform.

2.3. Decoration of Pt NPs on the TiO₂ NBs and MoS₂/TiO₂ NB heterostructures

50 mg of MoS₂/TiO₂ powder was dispersed in 100 ml of MQ water in an ultrasonic bath for 30 min. 52 mg H₂PtCl₆ was dissolved in 100 ml of MQ water and added drop-wise into the MoS₂/TiO₂ dispersion under magnetic stirring. Then, 50 ml of 0.01 M aqueous NaBH₄ solution was added slowly to the above mixture to deposit Pt NPs uniformly over the TiO₂ as well as MoS₂/TiO₂ HSSs.

2.4. Characterization techniques

The crystal structure of the as-grown catalysts was studied using an X-ray powder diffractometer (XRD) pattern (Rigaku RINT 2500 TTRAX-III, Cu K α radiation). The crystallinity and phase composition of the as-synthesized NRs and the number of layers in MoS₂ have been confirmed using micro-Raman measurements (LabRam HR800, Jobin Yvon). The morphology and size of the as-synthesized TiO₂ NBs and MoS₂ layer on the TiO₂ NBs have been studied using a field emission scanning electron microscope (FESEM) (Sigma, Zeiss). The high-magnification surface morphologies and structures of the as-grown samples have been studied using a field emission transmission electron microscope (FETEM) (JEOL-JEM 2100F operated at 200 kV). Elemental mapping of various samples was recorded using the FETEM equipped with an energy dispersive X-ray (EDX) spectrometer. Samples for TEM analysis were prepared on a carbon-coated Cu grid of 400 mesh size (Pacific Grid, USA). In particular, the edge sites of MoS₂ layers and the selective decoration of Pt NPs were identified using bright field scanning transmission electron microscopy (STEM) mode using an aberration-corrected STEM (JEM 2100F, 200 kV) and corresponding energy-dispersive X-ray spectroscopy (EDS) hypermaps were recorded to analyze the local environment of S, Mo, and Pt in TiO₂-based MoS₂ nanoflowers and Pt NP modified nanostructures. UV-vis diffuse reflectance spectroscopy (DRS) measurements were recorded using a commercial spectrophotometer (SHIMADZU 2600). Room temperature steady state PL spectra of the catalysts were recorded with the help of a spectrometer (focal length: 15 cm; blaze wavelength: 500 nm; groove density: 150 g mm⁻¹) equipped with a cooled charge-coupled device (Princeton Instruments, PIXIS 100B) detector using 405 nm diode laser (Coherent, Cube) excitation. X-ray photoelectron spectroscopy (XPS) has been carried out using a PHI X-tool automated photoelectron spectrometer (ULVAC-PHI, Japan) with an Al K α X-ray beam (1486.6 eV) at a beam current of 20 mA. The shift in

the binding energy of various catalysts has been corrected using the C1s spectrum at 284.8 eV as a standard value.¹²

2.5. Photoelectrocatalysis measurements under visible light

Photoelectrochemical measurements were performed systematically in a conventional three-electrode electrochemical cell: a commercial Ag/AgCl (saturated KCl) electrode (CH instruments) as the reference electrode, Pt wire or a graphite rod as the counter electrode and the as-grown catalysts supported on a glassy carbon substrate were used as working electrodes. Prior to catalyst loading, the surface of the glassy carbon substrate is polished with 50 μ m alumina powder on a polishing cloth and washed with DI water. 4 mg of catalyst was dissolved in 1 ml DI water and the dispersion was sonicated for 1 h. 6 μ L of the as-prepared sample was drop cast on the glassy carbon electrode (diameter = 3 mm) and dried in an inert atmosphere. The net loading of each catalyst is \sim 0.34 mg cm⁻². The electrochemical surface area (ECSA) of each catalyst was measured using the Randles-Sevcik equation:

$$I_p = (2.69 \times 10^5)n^{3/2}AD^{1/2}\nu^{1/2}C,$$

where I_p is the anodic peak current (amperes), ν is the scan rate of potential, n is the number of electrons involved in the reaction, A is the active surface area (cm²), C (mol cm⁻³) is the concentration of electroactive species, and D is the diffusion coefficient (cm² s⁻¹). Thus, the active surface area 'A' of the electrode is calculated from the cyclic voltammetry (CV) response of 5 mM [Fe(CN)₆]^{3-/4-} in 0.1 M KCl at different scan rates. The calculated ECSA for the TB, MS, PMS, PTB, MSTB and PMSTB are 0.038, 0.042, 0.048, 0.050, 0.052 and 0.045 cm², respectively.

Photo-electrocatalytic studies were performed using a Bio-Logic SP-300 electrochemical workstation. A 250 W Xenon lamp (Lelesil Innovative Systems, India) was used as the visible light source with a wavelength range of \sim 370–730 nm during the photoelectrochemical measurements. A 0.5 M H₂SO₄ solution was used as an electrolyte, deaerated by N₂ purging until saturation prior to any electrochemical experiment. Linear sweep voltammetry (LSV) was conducted at a scan rate of 5 mV s⁻¹. Electrochemical impedance spectroscopy (EIS) was also performed in 0.5 M H₂SO₄ under dark and light conditions at the HER onset potential of each catalyst over the frequency range 7 MHz–100 Hz with an input sine wave having 10 mV amplitude.

3. Results and discussion

3.1. Morphology studies

Fig. 1(a) shows a FESEM image of pristine TiO₂ NBs with a diameter of \sim 30–100 nm and length of \sim a few μ m, while Fig. 1(b) shows uniform decoration of Pt NPs over the TiO₂ NBs. During the 2nd stage hydrothermal treatment, self-assembly of few-layer MoS₂ nanosheets on the porous TiO₂ NB template transforms it into discrete MoS₂ nanoflowers (NFs) decorated on the TiO₂ NBs with the size distribution of 130–350 nm, as shown in Fig. 1(c). Fig. 1(d) shows the FESEM micrograph of Pt

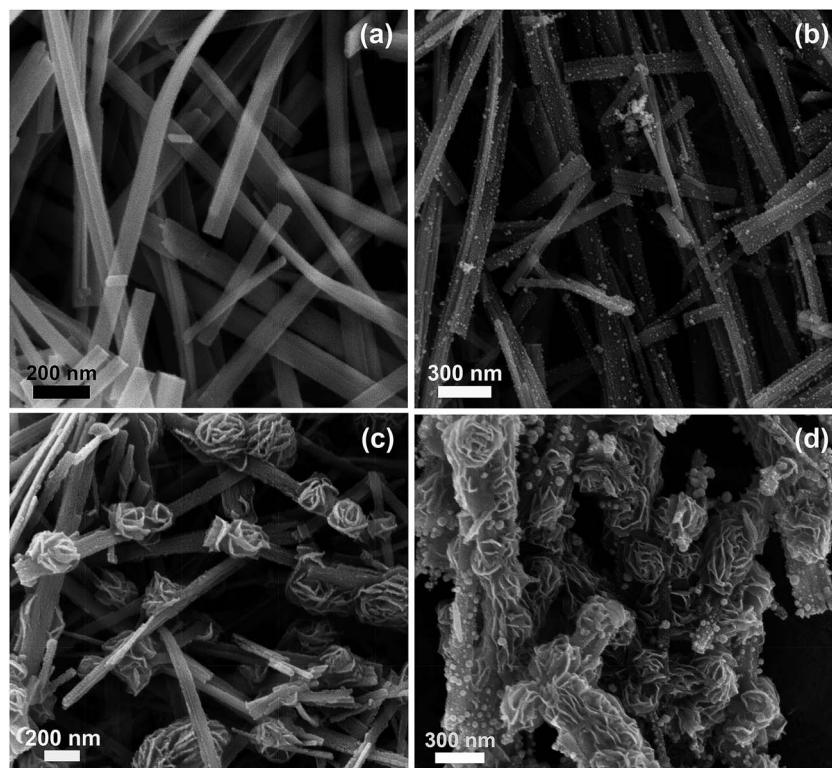


Fig. 1 FESEM images of (a) pristine TiO_2 NBs, (b) Pt NP decorated TiO_2 NBs, (c) MoS_2 NFs decorated on TiO_2 NBs, and (d) Pt NP decorated $\text{MoS}_2/\text{TiO}_2$ HSs.

NP-decorated MSTB HSs. Large Pt NPs can be observed on the TiO_2 surface maybe due to the aggregation. Note that, the deposited Pt NPs on the edge-exposed MoS_2 NFs have appreciably small size and a narrow size distribution (discussed later), and hence the NPs were not discernable here due to the resolution limit of FESEM.

Fig. 2(a and b) show TEM micrographs of Pt NPs decorated on TiO_2 NBs (PTB HS) at two different magnifications, demonstrating overall uniform decoration of Pt NPs, and Fig. 2(c) shows an HRTEM lattice fringe pattern of well-crystalline Pt NPs and TiO_2 NBs in PTB. The calculated lattice spacing of 0.22 nm corresponds to the (111) plane of Pt NP, and 0.29 nm and 0.32 nm correspond to the (111) and (002) crystal planes of $\text{TiO}_2(\text{B})$, respectively, in the PTB HSs. TEM images in Fig. 2(d and e) reveal the *in situ* growth of MoS_2 layers on the porous TiO_2 NB platform with a broad size distribution of 100–380 nm, which is in good agreement with the FESEM analysis. As evident from the images, the pure MoS_2 crystals with maximally exposed edge active sites appear to be layered wavy petals, and they gather together to form distinct nanorose-like structures on the porous TiO_2 NB platform due to the high autogenous pressure (~ 45 bar) inside the autoclave. Insets in Fig. 2(d and e) depict the hexagonal diffraction spots and a honeycomb atom arrangement in 2H- MoS_2 , respectively, grown over TB. Fig. S1(a and b) (ESI[†]) reveal the bright field STEM images of MSTB with different magnifications, showing the few-layer growth of MoS_2 over the porous structure of TiO_2 NBs.⁴⁶ The HRTEM lattice fringe pattern of MSTB HSs shown in Fig. 2(f) clearly reveals the co-existence of few-layer MoS_2 in the TiO_2 lattice. Fig. 2(f) shows

a typically layered nanosheet having ~ 6 sandwiched S-Mo-S layers with an interlayer spacing of ~ 0.67 nm. Additional ordered domains with a lattice spacing of 0.28 nm can be assigned to the (100) plane at the basal surface of 2H- MoS_2 . The lattice spacing of 0.37 nm, 0.39 nm, and 0.64 nm corresponds to the (110), (201) and (001) crystal planes, respectively, for the pure B-phase TiO_2 . It can be observed from the DF-STEM image of PMSTB shown in Fig. 2(g) that the Pt NPs are selectively decorated at the exposed edge sites of MoS_2 over the MSTB HS and the inset shows the size distribution of Pt NPs over the MSTB HSs. It shows a very narrow size distribution (distribution width ~ 0.19 nm) with an average size of 3.8 nm. Fig. 2(h and i) depict the dark field and bright field STEM images of Pt NPs anchored selectively on edge/defect sites of MoS_2 layers supported on the TiO_2 NBs, respectively.

In order to estimate the individual contribution of Pt NPs and MoS_2 on the HER under dark and light conditions, we performed STEM-EDS elemental mappings on the MSTB HSs before and after the modification with Pt NPs. Fig. 3(a) shows a STEM image of PMSTB on which elemental mapping was performed. EDS elemental mapping reveals that the core of the HS is composed of Ti and O elements, as shown in Fig. 3(b and c), which further confirms the uniform growth of TiO_2 . Fig. 3(d and e) show the elemental mapping for Mo and S, respectively, which supports our argument that the discrete MoS_2 NF grows on the TiO_2 platform as an outer layer. The Pt NPs are observed to be dispersed with overall uniformity over the MoS_2 NFs as confirmed by the elemental map of Pt shown in Fig. 3(f). Similar results of the elemental distribution of Ti, O as the core layer

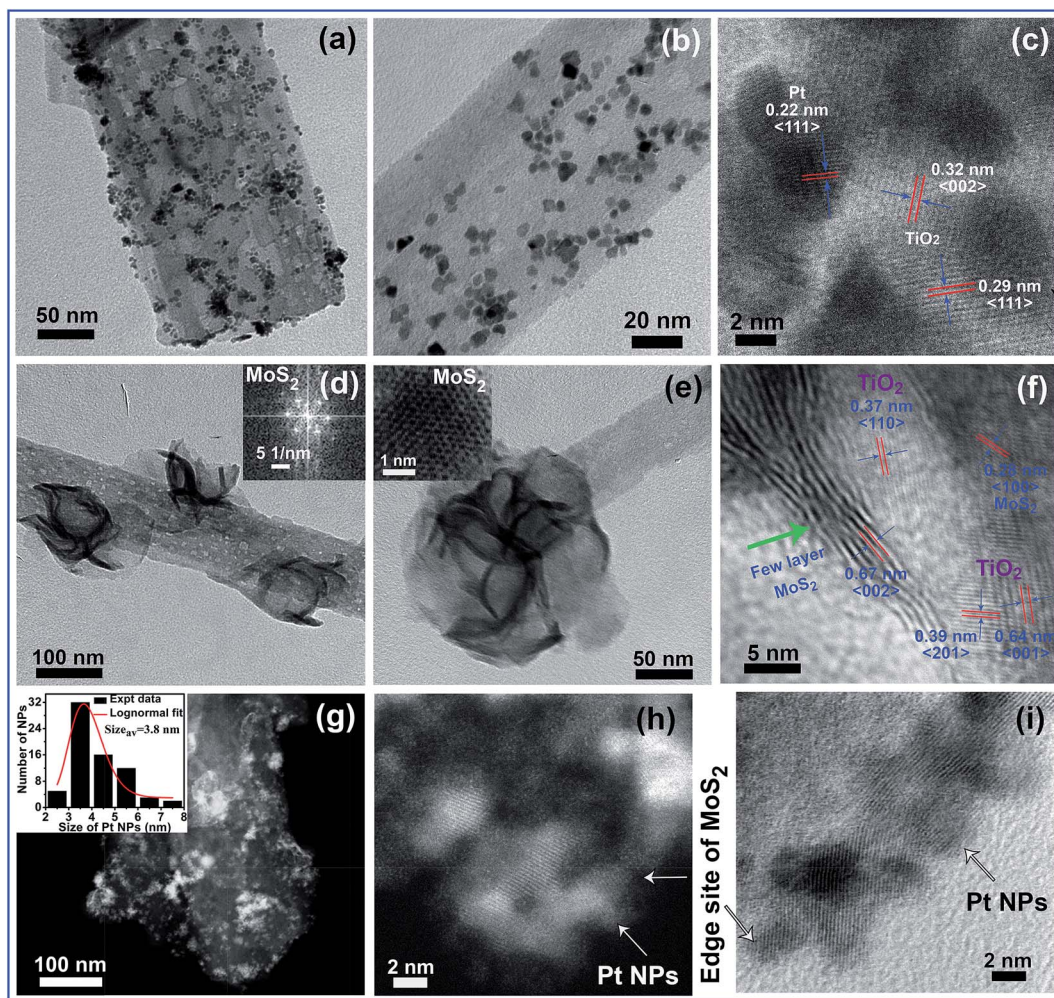


Fig. 2 (a and b) Pt NP decorated porous TiO₂ NBs at different magnifications, (c) HRTEM lattice fringe pattern showing the simultaneous presence of Pt and TiO₂. (d) TEM image of a MoS₂ NF decorated nanoporous TiO₂ NB; the inset shows the hexagonal diffraction spots on the NF site. (e) TEM image of a TiO₂ NB coated with MoS₂ NFs; the inset shows the BF-STEM image corresponding to the MoS₂ layer. (f) HRTEM lattice fringe pattern of MoS₂/TiO₂ HSSs. (g) HAADF image of Pt NPs decorated on MoS₂/TiO₂ HSSs. The inset shows the size distribution of Pt NPs decorated on MoS₂/TiO₂ HSSs and bright field STEM images of Pt NPs selectively decorated on the edge-sites of MoS₂ NFs, respectively.

and Mo and S as an outer layer were observed in the case of MSTB, as shown in Fig. S2(a–f) (ESI†). EDS spectra corresponding to MSTB and PMSTB shown in Fig. S2(g and h) (ESI†) confirmed that the ratio of S and Mo is found to be similar before and after Pt loading onto the MSTB HS (see Fig. S2(g and h), ESI†). It is clear that the majority of the Pt NPs is embedded at the edge sites of the 2H phase MoS₂ layers. The weight% of S is found to be high indicating S-rich MoS₂ layers in all the catalysts MS to MSTB to PMSTB, as evident from the EDS analysis of pristine samples (see Fig. S3, ESI†) which is reported to be beneficial for the enhanced HER activity.²² However, in the case of PTB, most of the Pt NPs are preferentially attached to the porous sites of TiO₂ nanostructures.

3.2. Structural analysis

3.2.1. XRD analysis. Fig. S4 (ESI†) depicts the XRD pattern of the as-grown catalysts. The diffraction peaks for pristine MoS₂ (marked with “*”) in Fig. S4(a) (ESI†) detected at $2\theta \approx$

14.5° , 32.9° and 56.5° can be attributed to the (002), (100) and (106) crystal planes, respectively (JCPDS card no. 37-1492). XRD peaks corresponding to pristine TiO₂ NBs (labeled with “♦”) match with the standard values of the TiO₂ monoclinic structure.¹² Fig. S4(c) (ESI†) shows the diffraction pattern of few-layer MoS₂ designed on porous TiO₂ NBs (MSTB). It can be noted that the diffraction peak of pristine MoS₂ at $\sim 14.5^\circ$ corresponding to the *c*-plane was not detected in the case of MSTB. Thus, the absence of this peak confirms the coating of TiO₂ NBs with extremely thin few-layer MoS₂ nanosheets, which may prevent the crystal growth along the *c*-axis. Fig. S4(d) (ESI†) shows the XRD pattern of PMSTB, which clearly confirms the co-existence of Pt, MoS₂, and TiO₂(B) crystals. In the figure, Pt has been depicted by circles (filled). The diffraction peaks of Pt are relatively sharp, clearly implying its highly crystalline nature.

3.2.2. Raman analysis. In order to investigate the crystallinity, phase and layer numbers in the as-grown catalysts, micro-Raman analysis has been conducted, as shown in Fig. 4. Each of

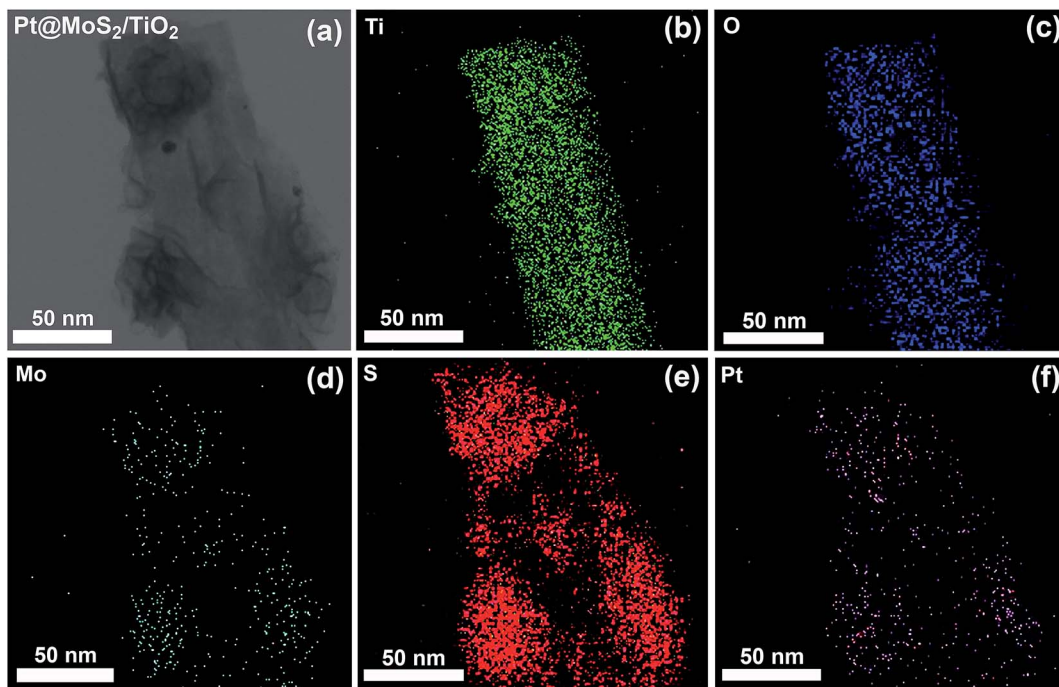


Fig. 3 STEM elemental mappings of PMSTB HS: (a) a raw image of the HS and (b–f) elemental maps of Ti, O, Mo, S and Pt, respectively.

the phonon modes of TiO_2 NBs correspond to the monoclinic structure of B-phase TiO_2 , see Fig. 4(a). The pristine MoS_2 exhibits two active Raman modes attributed to E_{2g}^1 and A_{1g} having a separation of 25.1 cm^{-1} , as shown in Fig. 4(a). However, MSTB exhibits a combination of B-phase TiO_2 and MoS_2 . In MSTB, these Raman modes are observed with a reduced separation of 22.3 cm^{-1} , as clarified by the vertical dotted lines. After loading the Pt NPs on MSTB, the intensity of

the characteristic MoS_2 peaks is significantly reduced, while that of TiO_2 is not affected much. This may be due to the screening effect of Pt NPs decorated over the edge-rich MoS_2 NFs. Fig. 4(b) shows the B_g and A_g Raman modes for B-phase TiO_2 in the pristine TB, MSTB, and PMSTB, and their corresponding Lorentzian fittings. It is evident that the intensity of TiO_2 Raman modes decreases after the decoration of MoS_2 , which may be due to the bonding of MoS_2 at the porous sites of

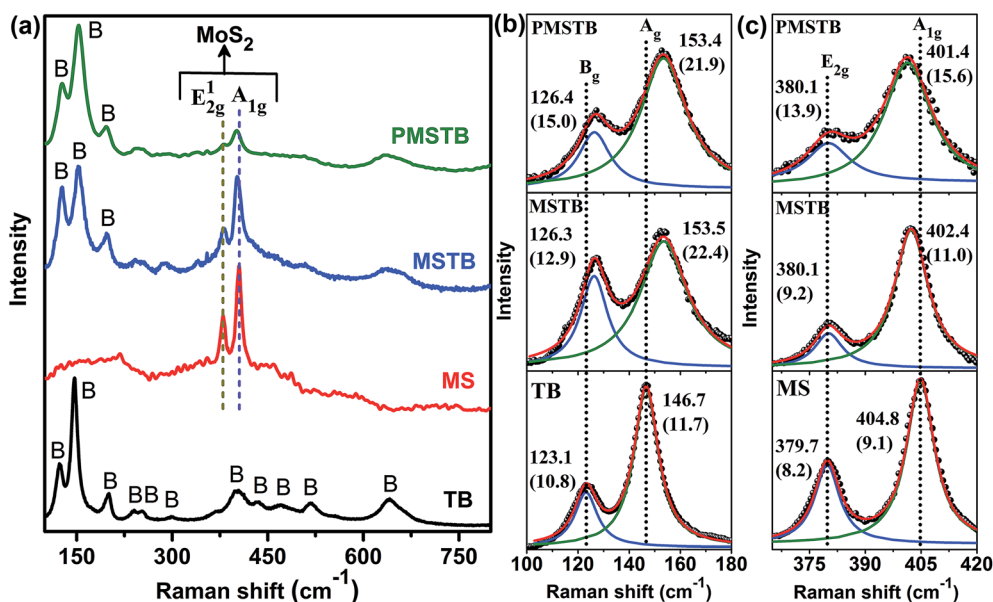


Fig. 4 (a) Raman spectra of pristine $\text{TiO}_2(\text{B})$ NBs, bare MoS_2 NFs, few-layer MoS_2 NF decorated $\text{TiO}_2(\text{B})$ NBs and Pt loaded $\text{MoS}_2/\text{TiO}_2$ HSs. (b) Lorentzian fittings of Raman spectra for TB, MSTB and PMSTB in the range of $100-180 \text{ cm}^{-1}$. (c) Lorentzian fittings of active Raman modes of MoS_2 corresponding to the bare MoS_2 , MSTB and PMSTB ($360-420 \text{ cm}^{-1}$). The vertical dotted lines indicate the position of the standard Raman mode of pristine MoS_2 and $\text{TiO}_2(\text{B})$.

TiO₂ NBs. The B_g and A_g Raman modes of TiO₂ NBs at 123.1 cm⁻¹ and 146.7 cm⁻¹, respectively, are broadened and blue shifted after the MoS₂ growth, as shown in Fig. 4(b). The MSTB shows a blue shift of 3.2 cm⁻¹ in B_g mode with broadening in the FWHM from 10.8 cm⁻¹ to 12.9 cm⁻¹. Similarly, for A_g mode, the MSTB HS exhibits a huge blue shift of 6.8 cm⁻¹ with an increment in the FWHM from 11.7 cm⁻¹ to 22.4 cm⁻¹. Such a large blue shift and broadening are mostly due to a surface strain (compressive type) induced by the MoS₂ nanosheets covered on the TiO₂ surface originating from the nonstoichiometric oxygen vacancy (O_v) defects resulting possibly from the S-doping at the O-site in the TiO₂ lattice.^{14,47,48} After the loading of Pt NPs over MSTB, no further increase of defect concentration in the TiO₂ lattice is observed. Fig. 4(c) shows the E_{2g} and A_{1g} Raman modes for MoS₂ in the pristine MS, MSTB, and PMSTB, and the corresponding Lorentzian fittings are also shown. The pristine MoS₂ exhibits two active Raman modes centered at 379.7 cm⁻¹ and 404.8 cm⁻¹, which are attributed to E_{2g}¹ and A_{1g} modes, respectively, as shown in Fig. 4(c). However, in MSTB, these Raman modes are observed at 380.1 cm⁻¹ and 402.4 cm⁻¹, respectively.^{28,49} The former peak (E_{2g}¹) is attributed to the in-plane vibrations and the latter one (A_{1g}) to the vertical-plane vibrations in the Mo–S bond of MoS₂ and the separation between these two peaks is mainly determined by the layer number in MoS₂ nanosheets.⁵⁰ The estimated frequency differences between these two modes are $\Delta\nu \approx 25.1$ cm⁻¹ and 22.3 cm⁻¹ for pristine MS and MSTB, respectively. Thus, the growth of few-layer pristine MoS₂ is confirmed and the reduction in $\Delta\nu$ for MSTB may be interpreted as follows: first, the overall growth of layered MoS₂ on the TiO₂ platform leads to a reduced number of layers (bilayer/few-layer); this is due to the presence of numerous porous nucleation sites in TiO₂ NBs which not only act as the nucleation sites for the growth of layered MoS₂, but also constrain their aggregation to yield bilayer/few-layered structures. In contrast, the bare MoS₂ NFs aggregate during the hydrothermal growth due to the absence of any anchoring support, resulting in multilayered MoS₂. Second, in MSTB, the only A_{1g} peak is observed to be redshifted (by ~ 2.4 cm⁻¹), whereas the E_{2g} peak remained unchanged. This may be due to the softening of A_{1g} vibrations at high electron concentrations, which results from the n-type doping in MoS₂ grown in the vicinity of S-doped and O_v enriched TiO₂.^{51,52} In PMSTB, the A_{1g} mode exhibits a further redshift of 1 cm⁻¹ with a larger FWHM, indicating the n-doping effect in the MoS₂ lattice. This can be understood from the band bending at the interfaces of MoS₂ and TiO₂, facilitating the electron transfer from the TiO₂ to the MoS₂ side, which will be discussed later.

3.2.3. XPS analysis. The chemical valence state, the stoichiometric ratio of the systems and the surface defects present in pristine catalysts and their HS were investigated by the XPS analysis. The Ti 2p core level XPS spectra of pristine TB were deconvoluted by Gaussian fitting to determine the double peak features of Ti 2p_{3/2} and Ti 2p_{1/2}, as shown in Fig. S5(a) (ESI[†]). The fitted peaks corresponding to the binding energies of 458.8 and 464.5 eV can be attributed to Ti⁴⁺ cation. Two additional Gaussian peaks centered at 456.7 eV and 461.0 eV related to the Ti³⁺ valence state were detected with a relative percentage of

4.9% for TB, which reveals the presence of nonstoichiometric O_v defects in the system.¹² Fig. S5(b) (ESI[†]) shows the Pt 4f core level XPS spectrum for the PMSTB, which can be deconvoluted into four symmetric Gaussian peaks, corresponding to the two different valence states of Pt. The Pt 4f_{7/2} and Pt 4f_{5/2} peaks detected at 71.5 eV and 74.8 eV, respectively, originate from metallic Pt⁰, while the other pair at 72.7 and 76.4 eV correspond to Pt 4f_{7/2} and Pt 4f_{5/2} of Pt²⁺, respectively.^{53,54} The area under each peak reveals the relative atomic percentage of Pt⁰ and Pt²⁺ as 75.8% and 24.2%, respectively, in PMSTB, signifying that the Pt is mainly in the metallic state. The additional Pt²⁺ in the HS sample may form Pt–O bonds due to the chemisorption of oxygen and hydroxyl groups on the surface of the Pt NP and MoS₂ layers. Fig. S5(c and d) (ESI[†]) depicts the Mo 3d core-level XPS spectra of MSTB and PMSTB, respectively. The strongest Mo 3d doublet peaks for MSTB detected at 229.2 eV (3d_{5/2}) and 232.5 eV (3d_{3/2}) shown in Fig. S5(c) correspond to the +4 oxidation state of Mo, confirming the formation of MoS₂. The shoulder peaks detected at 226.4 eV and 235.7 eV can be attributed to the S 2s state and Mo⁶⁺ oxidation state, probably due to the formation of MoO₃ during the hydrothermal growth and post-synthesis exposure to air. After the Pt NP decoration on MSTB, the major Mo 3d doublet peaks corresponding to the +4 valence state have been detected at 229.7 eV (3d_{5/2}) and 232.9 eV (3d_{3/2}). Each of the peak shifts by ~ 0.5 eV towards the higher binding energy side, which may be due to the distortion in the mixed state Mo arising from the generation of oxygen deficiencies in the system as evident from the absence of the Mo⁶⁺ oxidation state.

To characterize the nature of S atoms present in the catalysts, which are responsible for their HER activity, the core level XPS spectra of S were recorded and the results are shown in Fig. 5 and the corresponding area percentage is shown in Table 1. The pristine MoS₂ layers contain S atoms with electron binding energies at $\sim 161.9/163.1$ eV and $\sim 163.4/164.6$ eV, respectively (two sets of doublets), as shown in Fig. 5(a). The lower binding energy doublets are assigned to unsaturated S²⁻ and terminal S₂²⁻, while the higher binding energy doublets are assigned to bridging S₂²⁻ and apical S²⁻.⁵⁵ In addition to the formation of MoS₂, the presence of S²⁻ in the HS sample may correspond to the Ti–S bond formed during the substitution of O-atoms by S-atoms in the TiO₂ crystal lattice, resulting in S-doped TiO₂, which is consistent with the large blue shift in TiO₂ Raman spectra and enhancement of O_v concentration in the TiO₂ lattice after the *in situ* growth of MoS₂ over TiO₂ (discussed later).^{47,48} Ting *et al.*⁵⁵ demonstrated that the catalytic reactivity, as well as the turnover frequency of hydrogen production, increases almost linearly with increasing the amount of bridging S₂²⁻/apical S²⁻ in the catalysts. In the present case, pristine MS exhibits S atoms with bridging S₂²⁻/apical S²⁻ as 39.1% which is found to be increased to 54.4%, after its growth on porous TB, as shown in Fig. 5(a and b). Therefore, the TB NBs not only facilitate the few-layer growth of MoS₂ with edge-exposed sites but also serve as an effective platform for mediating the evolution of MoS₂ with more bridging S₂²⁻/apical S²⁻ to promote the enhanced HER activity. It is noteworthy that after Pt NP decoration on MSTB, the bridging S₂²⁻/apical S²⁻ increases dramatically to 72.2%, as shown in Fig. 5(c). Thus, it is

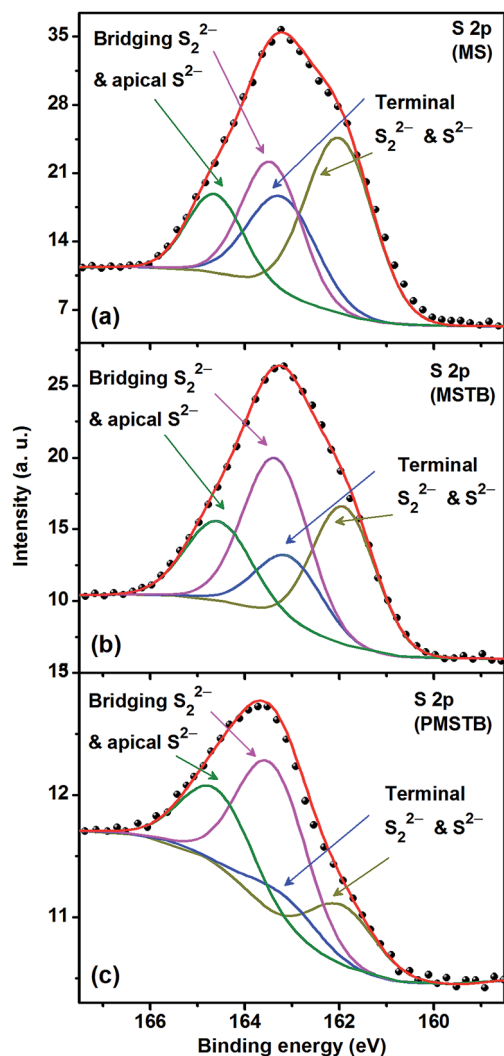


Fig. 5 S 2p core level XPS spectra of (a) MS, (b) MSTB and (c) PMSTB, fitted with the Shirley baseline. The symbols represent the experimental data and the solid lines correspond to the Gaussian fits. Identity of each fitted peak is denoted with corresponding charge states in the respective cases.

clear that the Pt NPs plays a crucial role to increase the bridging S_2^{2-} /apical S^{2-} amount in the HS and eventually in the superior HER performance.⁵⁵

Fig. 6(a-d) displays the O 1s XPS spectra of TB, MSTB, PTB and PMSTB, respectively. The spectra corresponding to pristine TB and PTB possess a long tail towards the higher-energy region making the spectra asymmetric in nature. In addition, MSTB and PMSTB exhibit exceptionally broad O 1s spectra implying the presence of defects or impurities on its surface. Each O 1s spectra can be fitted with three symmetric Gaussian peaks, as reported in the literature.⁵⁶ The first peak at ~ 530.1 eV is attributed to the TiO_2 crystal lattice and its relative percentages are calculated to be 66.6%, 61.4%, 21.2% and 21.3% for TB, PTB, MSTB, and PMSTB, respectively. Thus, it is clear that the relative percentage of lattice oxygen in TiO_2 decreases marginally after the Pt decoration, but it decreases dramatically after the decoration of MoS_2 . The second peak at ~ 531.2 eV can be assigned to the Ti-O bond ($O_{Ti^{3+}}$) and the relative $O_{Ti^{3+}}$ calculated from the O 1s XPS spectra is tabulated in Table 1. After the decoration of MoS_2 , the O_V concentration in the TiO_2 lattice is observed to be more than doubled from 21.1% to 46.1%, which may be due to the substitution of O-atoms in TiO_2 with the S-atoms during the *in situ* growth of MoS_2 over the TiO_2 platform. This is consistent with the large blue shift in the Raman spectrum. Loading of Pt NPs on TB or MSTB results in the decrease in O_V concentration from its initial value, perhaps due to the presence of Pt^{2+} species, which reduce the vacancy concentration. The third peak at ~ 532.7 eV is attributed to the hydroxyl group adsorbed on the HS surfaces and its relative percentages are shown in Table 1. Thus, it is observed that introduction of Pt NPs into the nanostructures enhances the relative percentage of the adsorbed hydroxyl group from 12.3% to 23.1% for pristine TB and from 32.7% to 47.3% for MSTB. Thus, it can be concluded that the Pt NPs introduce the hygroscopic nature in the nanostructure and also increase the adsorption capability in the system. These exceptionally high defect states may serve as shallow donors and enhance the charge transfer at the multiple interfaces, which in turn improves the overall photoelectrocatalytic water splitting under solar light, as discussed later.

3.3. UV-vis absorption and photoluminescence study

To investigate the solar energy harvesting efficiency, the pristine and the HS catalysts were analyzed by UV-visible diffuse reflectance spectroscopy (DRS). Fig. 7(a) shows the Kubelka-Munk (K-M) function, $F(R)$, for each of the samples

Table 1 Summary of the samples, their effective band gap, the relative percentage of oxygen vacancies (O_V), hydroxyl groups (O_H), lower and higher binding energy (BE) S present in the samples

Sample code	Sample	Various species from deconvoluted XPS spectra (in%)			
		O_V	O_H	Lower BE S (terminal and unsaturated)	Higher BE S (bridging and apical)
TB	$TiO_2(B)$	22.2	18.4	—	—
MS	MoS_2	—	—	60.9	39.1
MSTB	MoS_2/TiO_2	46.1	32.7	45.6	54.4
PMS	$Pt@MoS_2$	—	—	—	—
PTB	$Pt@TiO_2$	15.5	23.1	—	—
PMSTB	$Pt@MoS_2/TiO_2$	31.4	47.3	27.8	72.8

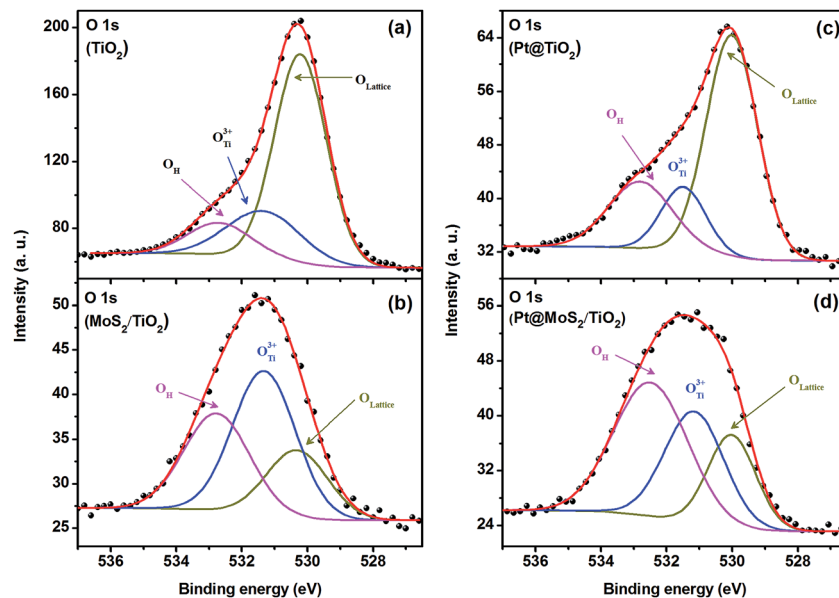


Fig. 6 O 1s core level XPS spectra of (a) TB, (b) MSTB, (c) PTB and (d) PMSTB with the Gaussian fit of each spectrum with the Shirley baseline. Symbols represent the experimental data and solid lines the Gaussian fits. Charge states associated with each peak are labeled in the spectrum.

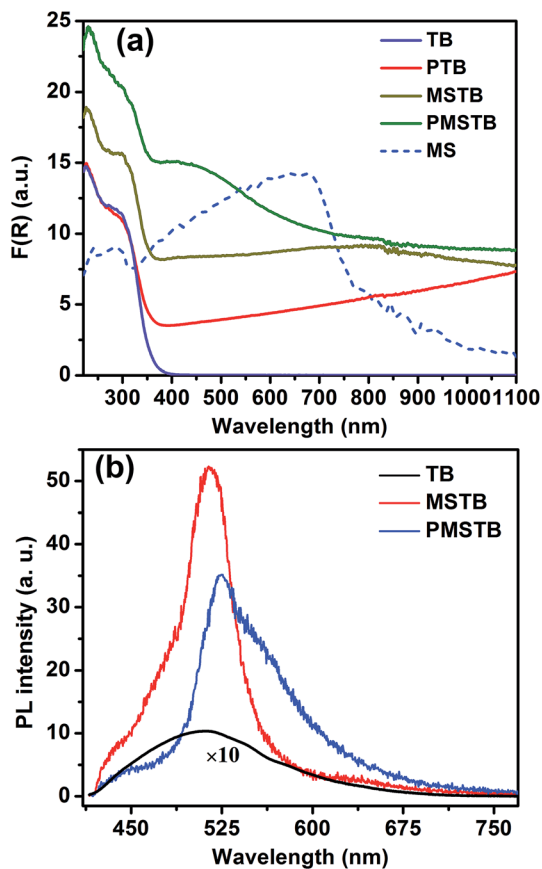


Fig. 7 (a) Kubelka–Munk plot, $F(R)$, for different samples derived from the diffuse reflectance spectra. (b) PL spectra of TiO_2 and its HSs measured with 405 nm laser excitation. The PL spectrum of TB is shown on a magnified scale to enable comparison.

corresponding to their DRS spectra. The pure $\text{TiO}_2(\text{B})$ NBs exhibit a sharp rise in absorption (edge) at ~ 360 nm (the indirect bandgap estimated from the Tauc plot is ~ 3.25 eV), which is attributed to their intrinsic band gap absorption. Pristine few-layer MoS_2 NFs exhibit a broad absorption band having a peak at ~ 670 nm (direct bandgap estimated from the Tauc plot: ~ 1.63 eV) showing a large blue shift compared to their bulk counterpart. This may be attributed to the strong quantum confinement effect of the thin and layered MoS_2 nanosheets, which makes the MoS_2 a promising candidate for visible light photocatalysis.⁵⁷ Incorporation of few-layer MoS_2 on TiO_2 NBs enhances the absorption intensity significantly over the wide UV-visible-IR range, as shown in Fig. 7(a). Introduction of Pt NPs on the TiO_2 NBs further enhances the visible light absorption efficiency, with a new absorption band centered at ~ 415 nm, besides its enhanced UV and visible-NIR absorption. Cueto *et al.*⁵⁸ have shown that Pt NPs with a size of 5–35 nm exhibit a plasmonic absorption covering a narrow band in the range 200–320 nm, and a broader band with a tail extending up to the NIR region. However, in the case of large Pt NPs the absorption band becomes intense and broad enough as a consequence of stronger plasmonic excitation due to the formation of numerous hotspots between two or more Pt NPs close to each other. In the present work, the Pt NPs decorated over the MoS_2 NFs are closely spaced, which enables high plasmonic excitation generation in the numerous hotspots, and results in high absorption. Interestingly, the absorption edge of the TiO_2 NBs is observed to be red shifted after decoration of MoS_2 NFs as well as Pt NPs. With Pt NPs, the absorption edge of the TiO_2 is red shifted to ~ 380 nm from ~ 360 nm. In the case of MSTB, it is further redshifted to ~ 402 nm, which implies an efficient band bending at the interface arising from the strong coupling between the porous TiO_2 and wrapped MoS_2 layers. S-

doping in the TiO_2 lattice may also be attributed to this red shift.⁴⁷ However, the maximum red shift is observed in PMSTB (~ 471 nm), which may be attributed to the strong coupling between each pair of the components MoS_2 -Pt, MoS_2 - TiO_2 , and Pt- TiO_2 . Thus, the HSs are expected to be extremely sensitive to the visible-NIR light and would be beneficial for the efficient visible light photoelectrocatalytic hydrogen evolution.

Fig. 7(b) shows a comparison of room temperature PL spectra of TB, MSTB, and PMSTB. Pristine TiO_2 NBs exhibit very weak and broad PL emission having an emission peak at ~ 515 nm, which is attributed to the single electron trapped oxygen vacancy (O_v) defects (F^+ center).^{56,59} After the growth of the MoS_2 layer on TiO_2 NBs, the PL intensity corresponding to the F^+ center increases strongly, indicating an increase in the concentration of O_v defects. During the *in situ* hydrothermal growth of MoS_2 on TiO_2 , S-atoms may diffuse and substitute the O-atoms in the TiO_2 lattice, causing S-doping in TiO_2 . This causes an increase in the O_v concentration and an eventual increase in electron density in TiO_2 . Due to the high optical absorption and O_v defects in MSTB HS, the PL intensity corresponding to the F^+ center increases substantially. After loading of Pt NPs over MSTB, the PL intensity reduces, which is due to the fast interfacial electron transfer from TiO_2 to Pt NPs *via* MoS_2 . Additionally, PMSTB shows a relatively broader PL spectrum indicating the contribution from the hydroxyl group attached to the TiO_2 surface, which is consistent with the XPS analysis.

3.4. Hydrogen evolution reaction (HER) study

The visible light HER performance of various catalysts, such as TB, MS, MSTB, PMS, PTB and PMSTB as working electrodes made on a glassy carbon disk was investigated in an N_2 -saturated 0.5 M H_2SO_4 solution using a typical three-electrode linear sweep voltammetry (LSV) method. For a better comparison, each measurement has been repeated under dark conditions as well. The electrochemical HER activities (LSVs) of various catalysts under dark and light conditions (wavelength range 370 – 730 nm) are shown in Fig. 8(a and b) and the corresponding Tafel slopes are shown in Fig. 8(c and d), respectively. Note that the results are nearly independent of scan rates in the range 2 – 10 mV s^{-1} (see Fig. S9 and Table S1, ESI[†]) and the presented data correspond to a scan rate of 5 mV s^{-1} . As shown in Fig. 8(a), the HER for pristine TiO_2 NBs starts at a potential of -623 mV and -616 mV (*versus* RHE) under dark and light conditions, respectively, above which the current increases drastically. In spite of very low overall current density, TB presents a HER overpotential (to attain -10 mA cm^{-2} current density) of -796 mV under light at a current density of 10 mA cm^{-2} , which is positively shifted by 87 mV as compared to that in the dark. The pristine few-layer MoS_2 exhibits much enhanced current density with a low onset potential of -246 mV, which reduces to -193 mV after light illumination. The overpotential is observed to be -425 mV and -395 mV under dark and light conditions, respectively (see Table 2). Interestingly, in MSTB the uniform decoration of edge-exposed few-layer MoS_2 on the porous sites

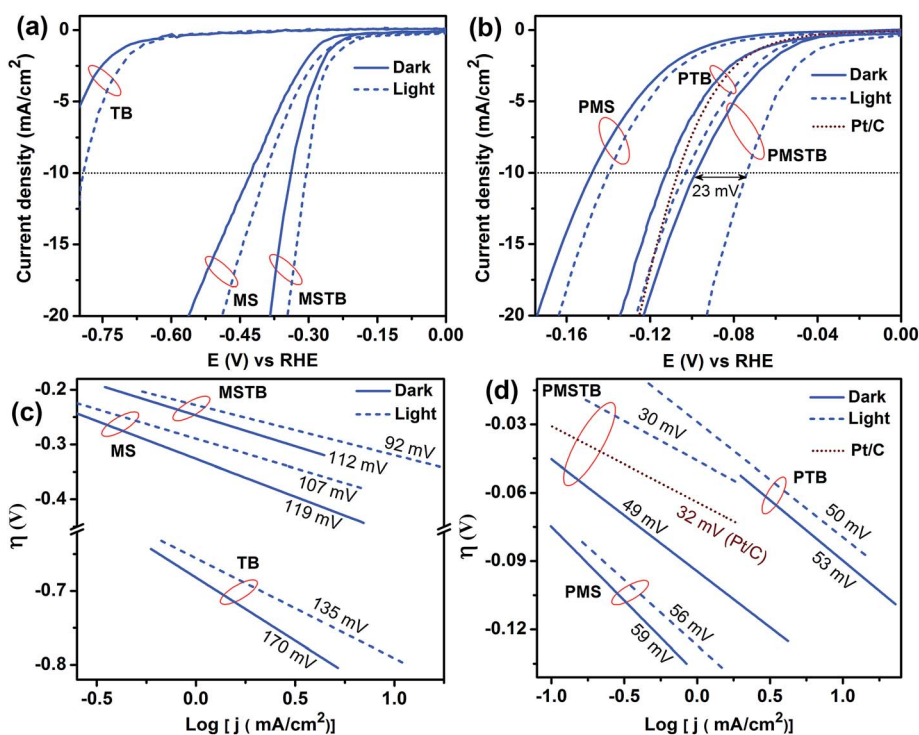


Fig. 8 Polarization curves of the hydrogen evolution reaction (HER) under dark and light conditions in (a) pristine TiO_2 (B), MoS_2 and $\text{MoS}_2/\text{TiO}_2$ (B) HS, (b) Pt@ MoS_2 , Pt@ TiO_2 and Pt@ $\text{MoS}_2/\text{TiO}_2$ HSs. (c and d) Tafel plots of different working electrodes derived from their LSV curves shown in (a and b), respectively. Polarization curve and the corresponding Tafel plot for the Pt/C electrode are also shown in (b and d), respectively.

Table 2 Comparison of various catalytic parameters of different photocatalysts under dark and light conditions

Catalyst code	Onset potential (at -0.5 mA cm^{-2}) [(mV) V RHE]		Overpotential at -10 mA cm^{-2} [(mV) V RHE]		Tafel slope (mV dec^{-1})		Charge transfer resistance, R_{ct} (Ω)		Exchange current density, j_0 (mA cm^{-2})	
	Dark	Light	Dark	Light	Dark	Light	Dark	Light	Dark	Light
TB	-623	-616	-883	-796	170	135	527	450	0.001	0.002
MS	-246	-193	-425	-395	119	107	132	121	0.008	0.013
MSTB	-215	-178	-336	-305	112	92	102	88	0.012	0.019
PMS	-76	-66	-147	-140	59	56	36	31	0.164	0.193
PTB	-45	-41	-113	-105	53	50	33	27	0.175	0.209
PMSTB	-40	-9	-97	-74	49	30	27	14	0.182	0.296
Pt/C	-48	—	-106	—	32	—	6	—	0.305	—

of TiO_2 NBs decreases the onset potential to -215 mV in the dark, which further reduces to -178 mV after irradiation with visible light as compared to those of bare TiO_2 and MoS_2 nanostructures. In MSTB, the overpotentials are calculated to be -336 mV and -305 mV under dark and light conditions, respectively. Thus, it can be concluded that more carriers are being generated in MSTB with light irradiation, which augments the reduction process of electroadsorbed protons. The introduction of merely $\sim 1.4 \text{ wt\%}$ Pt NPs on the TB, MS, and MSTB results in a dramatic reduction in the onset potential towards the HER. For PMS, it is measured to be -76 mV and -66 mV , while for PTB it is observed at -45 mV and -41 mV , under dark and light conditions, respectively. In the case of PMSTB, the onset potential in the dark is measured to be -40 mV , which is dramatically reduced to -9 mV after light irradiation, which essentially outperforms the commercial Pt/C electrode (-48 mV) with much higher Pt content. The summary of the performance of various catalysts is presented in Table 2. As evident from the table, the PMSTB exhibits exceptionally low overpotential under light, -74 mV , which is much lower (by 23 mV) than the value measured in the dark (-97 mV) and this is further lower than that of the commercial Pt/C electrode (-106 mV). Thus, a dramatic enhancement in the photogenerated charge carriers, as well as reduced charge transfer resistance, is expected in the systems after the Pt NP decoration, which serve as favorable nodes with large electron-accepting and buffering properties to facilitate electron transport, which in turn improves the overall conductivity.⁴

Tafel slopes of all the samples under both dark and light conditions (in mV per decade), estimated from the linear fit of the overpotential and logarithmic function of current density ($\log|j|$), are shown in Fig. 8(c and d) and tabulated in Table 2. Lower Tafel slopes not only reveal about the rate-determining step of the hydrogen evolution electrocatalysis mechanism but are also desirable to minimize the energy input required to achieve a targeted HER current density. From Fig. 8(c and d), it is evident that in each catalyst the Tafel slope decreases after the illumination with light compared to their respective dark values, which eventually confirms the acceleration of the electron transfer kinetics upon irradiation. In the dark, a much lower Tafel slope is estimated for pristine MS (119 mV dec^{-1}) than for pristine TB (170 mV dec^{-1}), which further decreases in

their composite system (MSTB) to 112 mV dec^{-1} . Under visible light illumination, their corresponding values are calculated to be 135 mV dec^{-1} (TB), 107 mV dec^{-1} (MS) and 92 mV dec^{-1} (MSTB), as shown in Table 2. After Pt NP loading on MS, TB, and MSTB, the Tafel slope is observed to be decreased drastically, as shown in Fig. 8(d). Tafel slopes for PMS and PTB are 59 and 53 mV dec^{-1} in the dark, and 56 and 50 mV dec^{-1} under light, respectively. PMSTB exhibits an exceptionally low Tafel slope (30 mV dec^{-1}) under light, which is much lower (19 mV dec^{-1}) than the value measured in the dark (49 mV dec^{-1}) and our values are comparable/better than that of a commercial Pt/C electrode (32 mV dec^{-1}). Two main reaction pathways are widely accepted in HER electrocatalysis, commencing with a primary discharge step (*i.e.*, Volmer reaction: $\text{H}_3\text{O}^+ + \text{e}^- \rightarrow \text{H}_{\text{adsorbed}}$), followed by either an electrochemical desorption step (*i.e.*, Heyrovsky reaction: $\text{H}_3\text{O}^+ + \text{e}^- + \text{H}_{\text{adsorbed}} \rightarrow \text{H}_2$) or a monoatomic hydrogen recombination step (*i.e.*, Tafel reaction: $\text{H}_{\text{adsorbed}} + \text{H}_{\text{adsorbed}} \rightarrow \text{H}_2$). As broadly reported in the literature, Tafel slopes of $\sim 120 \text{ mV dec}^{-1}$, $\sim 40 \text{ mV dec}^{-1}$, and $\sim 30 \text{ mV dec}^{-1}$ are allocated to Volmer, Heyrovsky and Tafel reactions being the HER rate-determining step, respectively.^{60,61} In our case, the Tafel slopes of all the HS photocatalysts (MSTB, PMS, PTB, and PMSTB) fall between the Volmer mechanism and the Tafel mechanism indicating that the Volmer-Tafel mechanism plays the predominant role in the catalysts' HER kinetics.⁶² The lowest Tafel slope found for PMSTB under visible light illumination (*i.e.* enhanced HER kinetics) consequently supports its high HER performance.

Electrochemical impedance spectroscopy (EIS) is a powerful technique to characterize interface reactions and the heterogeneous electron transfer process in HER.⁶³ Fig. 9(a-d) and S7(a and b) (ESI[†]) show the Nyquist plots of all the samples corresponding to their EIS response. The charge transfer resistance (R_{ct}) values have been calculated for all the samples estimated from the Randles circuit (see Fig. S7(c), ESI[†]) under dark and light conditions.⁶⁴ In the dark, the R_{ct} is calculated to be lower for MSTB (102Ω) as compared to those of the pristine TB (527Ω) and MS (132Ω). Interestingly, after the Pt NP decoration, the R_{ct} dramatically reduces to 36Ω , 33Ω and 27Ω for PMS, PTB, and PMSTB, respectively, in the dark. The R_{ct} values of all catalysts are decreased even further upon illumination, indicating the presence of photogenerated carriers in these

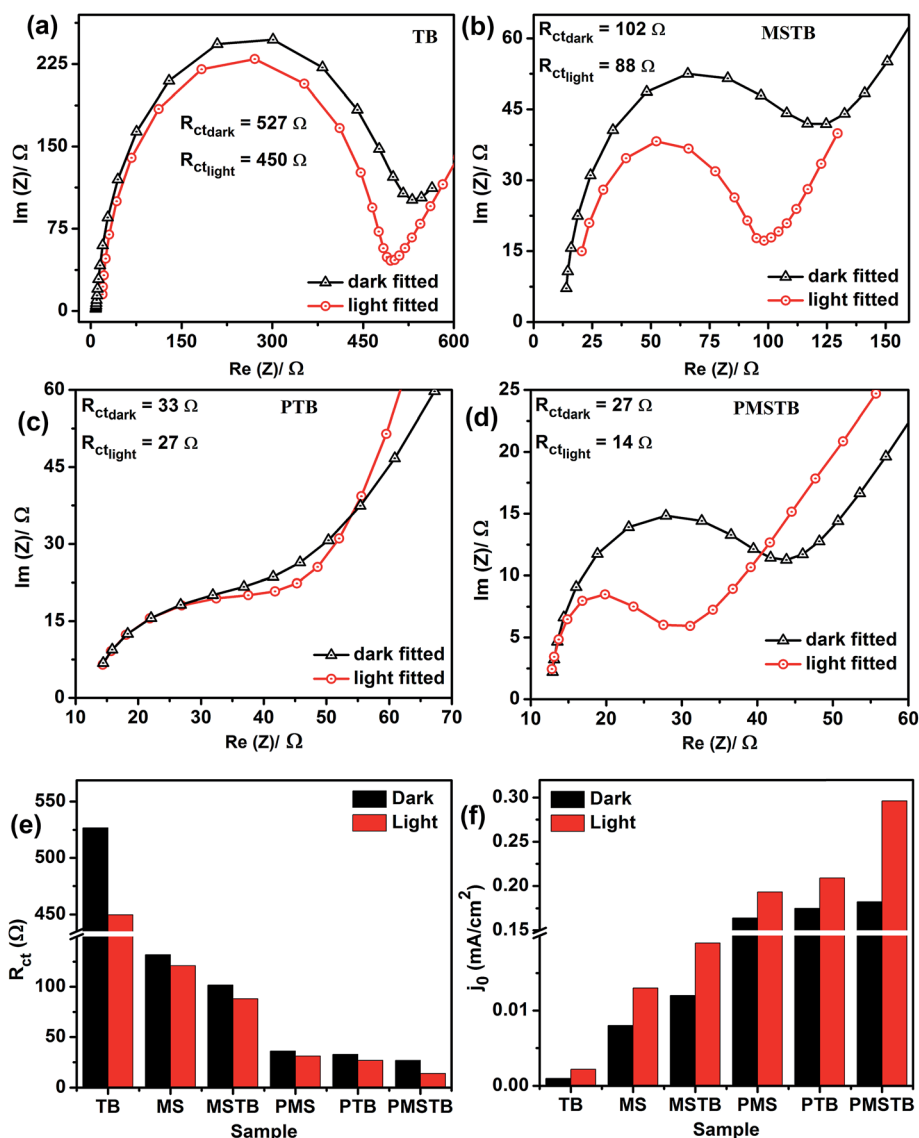


Fig. 9 Nyquist plots of (a) pristine $\text{TiO}_2(\text{B})$, (b) $\text{MoS}_2/\text{TiO}_2$, (c) $\text{Pt}@/\text{TiO}_2$ and (d) $\text{Pt}@/\text{MoS}_2/\text{TiO}_2$ HSSs, under dark and light conditions. Note that the points represent experimental data, while the solid lines are simulation using the Randles circuit to estimate the characteristic charge-transfer resistance (R_{ct}). (e and f) R_{ct} and j_0 values, respectively, of various electrodes under dark and light conditions.

electrodes, as tabulated in Table 2 and Fig. 9(e). Under illumination, the R_{ct} for PMSTB decreases to the minimum value of 14 Ω indicating the augmented charge transfer process in the presence of light. The heavy n-type doping in the catalytically active edge-exposed MoS_2 NFs (as demonstrated from Raman analysis, see Fig. 4(c)) provides a fast electron transfer from the TiO_2 side to the MoS_2 side and results in superior HER kinetics, which is dramatically enhanced after the introduction of metallic and highly active catalyst Pt NPs into the MSTB system.

Further insight into the intrinsic activity of the HER electrocatalysts can be obtained by comparison of exchange current density (j_0) values, which is determined by the ability to exchange electrons from the working electrode to the counter electrode through the electrolyte solution at null potential. Fig. 9(f) compiles exchange current density, j_0 , values obtained under dark and light conditions for all studied samples. It is

noteworthy that a dramatic enhancement (~ 10 -fold) in j_0 value is observed in TB under visible light after the decoration with MoS_2 layers. Furthermore, for all samples tested, there is a significant increase in j_0 values after visible light illumination, consistent with the lower R_{ct} and Tafel slope values found after light irradiation. Among the various electrodes studied here, PMSTB showed the highest j_0 (~ 0.182 mA cm^{-2} in the dark and 0.296 mA cm^{-2} under visible light). Thus, the aforementioned enhanced HER performance of MSTB is a result of the efficient charge transport and favorable HER kinetics at the interface of the HS components, which is further enhanced after decoration with Pt NPs, widely regarded as the best performing noble metal catalyst for the HER.

To evaluate the durability of the as-prepared catalyst, the cyclic durability, as well as long term stability, was investigated, and the results are presented in Fig. 10(a). A long-term cycling

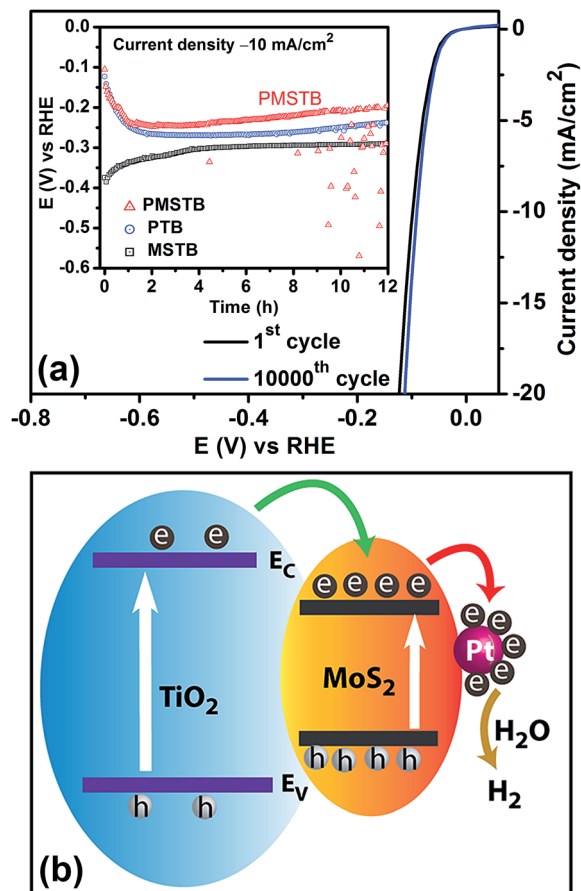


Fig. 10 (a) Polarization curves recorded for PMSTB before and after 10 000 CV cycles. The inset shows the chronopotentiometry showing the stability of the catalysts for 12 h at a sustained current density of -10 mA cm^{-2} . (b) Schematic illustration of charge transfer at the multiple interfaces of PMSTB and the mechanism of enhanced visible light PEC activity of Pt NPs decorated on TiO₂/MoS₂.

experiment (up to 22 hours) was performed for PMSTB by recording 10 000 cycles from 0 V to -0.2 V vs. RHE. As shown in Fig. 10(a), the polarization curve shows no loss in current density after 10 000 CV cycles, though the performance marginally improves with time, which may be due to the improved interfacial contact and possible Pt dissolution/redeposition at the PMSTB surface, which may yield an increase in the HER active sites. The long term stability test was performed by chronopotentiometry measurements to evaluate the catalyst capability of sustaining a 10 mA cm^{-2} cathodic current over a 12 h period (see inset of Fig. 10(a)). The catalyst PTB shows the initial decay of HER performance up to 3 h of operation ($-0.270 \text{ V}@3 \text{ h}$ vs. $-0.123 \text{ V}@0 \text{ h}$), indicating the stabilization of the anchoring effect of MoS₂ with respect to the decorated Pt NPs. Beyond 3 h, PTB performance marginally improves with time up to 12 h ($-0.238 \text{ V}@3 \text{ h}$). PMSTB shows a similar trend with an initial decay of HER performance with time up to 3 h, as shown in the inset of Fig. 10(a). Eventually, it reaches a HER performance of $-0.195 \text{ V}@12 \text{ h}$, which is better than that of PTB. Note that after 12 h of continuous galvanostatic operation at 10 mA cm^{-2} , the HER performance of PMSTB

decays by ~ 90 mV. Additionally, some intermittent fluctuation in the potential values is observed for PMSTB beyond ~ 4 h of continuous operation, which may be due to the mild oxidation of the MoS₂ sites accelerated by the anchored Pt NPs and the H₂ bubble movement. We cannot rule out the effect of leaching of the samples in MoS₂ and Pt-based ternary systems, which necessitates a more careful sample preparation for such experiments. Interestingly, the performance of MSTB initially improves with time and then reaches a saturation value. Possible coarsening of the MoS₂ layer along with electrochemical activation of the high binding energy S₂²⁻ sites upon irreversible HER cathodic cleaving may explain the observed enhancement.^{55,65} To understand the structural stability of the catalyst, the Raman spectra of MSTB were recorded before and after the PEC reaction. The crystallinity and stability of both TiO₂(B) and MoS₂ components are observed to be retained under the PEC reaction, as evident from Fig. S6 (ESI†). However, the relative intensity of MoS₂ characteristic peaks slightly decreases after the reaction, which may be due to oxidation and associated introduction of defects in the MoS₂ layers. One additional Raman peak is detected at $\sim 820 \text{ cm}^{-1}$ after the PEC reaction, which may be assigned to the M=O bond^{66,67} resulting from the marginal oxidation of MoS₂ in the acidic media. However, chronopotentiometric measurements show that the MSTB catalyst exhibits excellent stability towards HER activity up to 12 h, confirming the non-photocorrosive nature of our catalyst.

We believe that the interplay between Pt and MoS₂ interfaces, which ultimately results in enhanced HER performances, is not just the synergistic effect of Pt promotion of initially inactive MoS₂ sites and reduction in the TiO₂ bandgap, but also the mechanical anchoring provided by MoS₂ and the inherently high Pt HER electroactivity and conductivity. In addition, appropriate band bending at the multiple interfaces sweeps away the charge carriers and allows them to participate in the enhanced HER activity.

3.5. Mechanism of enhanced HER activity

Though MoS₂ is known as a catalytically active material, poor charge transport in the basal plane is often responsible for its inferior HER performance. Fabrication of edge-exposed MoS₂ and activation of the inert basal plane through Pt doping or extrinsic S vacancy generation have proven to be successful strategies to trigger superior HER electrocatalytic activities.⁶⁸⁻⁷⁰ In this study, few-layer MoS₂ with a high density of catalytically active edge-exposed sites is tightly coupled with the porous surface of S-doped TiO₂ NBs. Structural analysis by HRTEM and STEM imaging of the as-grown MoS₂ layers on the TiO₂ NBs confirms their edge-rich nature, and the presence of surface defects. This defect-rich structure leads to a higher exposure of unsaturated sulfur edge sites, which are widely regarded as the active sites responsible for the overall HER activity.^{22,55} Additionally, the MoS₂ layers grown onto the TiO₂ NB surface present an n-type doping of MoS₂, contributing to maximize HER activities after MoS₂ basal plane activation.

Upon illumination with visible light, electrons in TiO₂, as well as MoS₂ in the HSSs, may be excited, as confirmed by the UV-

1 visible absorption analysis. Due to the appropriate band align- 1
ment at the interface, the photogenerated electrons at the TiO₂ 2
NBs can easily be transferred to the MoS₂ layer, avoiding 3
possible recombination loss of carriers and it induces n-doping 4
of the MoS₂ layer, as depicted in Fig. 10(b). The photo action 5
spectra of different samples are shown in Fig. S8,† confirming 6
the visible light activation of electron–hole pairs and their effi- 7
cient separation. Consequently, this efficient charge transfer 8
occurring at the heterojunction (MSTB) greatly reduces the 9
charge transfer resistance under visible light (88 Ω) and 10
accounts for the enhanced exchange current density (j_0) under 11
illumination, which is measured to be 0.019 mA cm⁻². A 12
marginal amount of Pt NP (1.4 wt%) loading on the MSTB is 13
found to decorate the catalytically active edge sites of MoS₂ 14
as well as the porous sites of TiO₂ with Pt NPs. The enhanced HER 15
activities obtained after Pt decoration onto porous MoS₂ NFs/ 16
TiO₂ NBs indicate an even higher density of proton-accepting 17
sites compared to MoS₂ NFs/TiO₂ NBs, which presumably ar- 18
ises from further activation of initially electrocatalytically inert 19
MoS₂ basal planes and S-edge sites. In addition, the presence of 20
Pt NPs can also serve as advantageous metallic current collector 21
nodes to facilitate lower resistance transport pathways of photo- 22
excited electrons from TiO₂ domains to Pt NPs through MoS₂ 23
(see Fig. 10(b)), improving the overall conductivity.⁴ Hence, 24
significantly enhanced HER activity was observed using PMSTB 25
with a minimum charge transfer resistance of 14 Ω and a maximum 26
exchange current density of 0.296 mA cm⁻². Additionally, the 27
modification by H₂SO₄ decreases the work function of TiO₂, 28
which changes its conduction band offset.⁷¹ A schematic 29
illustration of the excitation of electrons and their separation 30
through two interfaces under the light irradiation is shown in 31
Fig. 10(b) and this results in the superior HER performance 32
of the composite system. The structural defects and porous S- 33
doped TiO₂ surface also promote a closer interaction between 34
MoS₂ and TiO₂ during solvothermal synthesis (*i.e.* higher 35
availability of nucleation sites), which may be responsible for 36
the catalytically active n-type doped structure of MoS₂ NFs. 37
The detection of hydrogen gas during the electrocatalysis 38
experiment and its quantification was made by the gas 39
chromatography measurement and the results are presented in 40
Fig. S10 and S11, respectively (ESI†).

On a separate note, the adsorbed hydroxyl group in the TiO₂ 41
lattice increases greatly after the decoration of MoS₂ layers 42
(32.7%), which further enhances to 47.3% after the loading of Pt 43
NPs on MSTB, as confirmed from XPS analysis. As the Volmer– 44
Tafel HER mechanism governs the HER performance in our HS 45
catalysts, the higher presence of hydroxyl groups at the PMSTB 46
electrode, known to facilitate electroadsorbed hydrogen 47
desorption, may promote the rate-limiting electrochemical 48
desorption step involving hydrogen gas formation. 49

4. Conclusion

55 In summary, a hierarchical Pt@MoS₂/TiO₂ HS has been 56
successfully grown *via* a three-step chemical process, which 57
consists of solvothermal fabrication of TiO₂(B) NBs, its surface 58
decoration by discrete few-layer MoS₂ by a hydrothermal 59

method followed by *in situ* decoration of Pt NPs onto it. Uniform 1
decoration of MoS₂ layers on the porous sites of TiO₂ as well as 2
preferential decoration of Pt NPs on edge-sites/defect-sites of 3
MoS₂ and porous sites of TiO₂ NBs has been evidenced by the 4
FETEM and STEM analyses. The maximally edge-exposed MoS₂ 5
NFs grown on and supported by the porous TiO₂ platform 6
exhibit overall reduced layer numbers compared to the pristine 7
MoS₂ layers and the MoS₂ NFs likely to be n-type doped, as 8
revealed from the Raman analysis. In the HSSs, MoS₂ exhibits 9
exposed edge-sites, considered as the active nodes towards the 10
HER. The formation of O_v rich MSTB and PMSTB with 11
extremely high and broad visible to NIR absorption has been 12
evidenced by the XPS and UV-visible absorption spectra, 13
respectively. XPS analysis shows that the catalytically active 14
bridging S₂²⁻/apical S²⁻ increases up to ~72% after the 15
formation of the ternary system, PMSTB. Formation of a well- 16
coupled heterojunction between MoS₂ and S-doped TiO₂ 17
accelerates the charge transfer rate from the TiO₂ to the MoS₂ 18
side through the interfaces. Interestingly, Pt NPs anchored with 19
the edge-sites of MoS₂ and porous sites of TiO₂ collect the 20
photo-excited carriers making the HSS superior for HER activity 21
than their individual counterparts. Under visible light illumi- 22
nation, the onset potential of MSTB is observed to be much 23
lower (−178 mV) than that of the TiO₂ (−616 mV) and MoS₂ 24
(−193 mV) layer, with significant enhancement in the exchange 25
current density. With the loading of 1.4 wt% Pt NPs on MSTB, 26
the onset potential and the corresponding Tafel slope are 27
reduced drastically to −9 mV and 30 mV dec⁻¹, respectively, 28
with dramatically improved exchange current density (0.296 mA 29
cm⁻²). The Pt NP-supported HSS exhibit a giant enhancement in 30
HER activity as evidenced by the EIS spectra. The presence of 31
edge-defect enriched few-layer MoS₂ NFs on porous TiO₂ NBs, 32
supported by a marginal amount of Pt NPs exhibit extremely 33
high hydrogen generation with high-performance stability at 34
the working electrode through the Volmer–Tafel mechanism. 35
Our results are very significant for the development of multi- 36
component catalysts. 37

Conflicts of interest

Acknowledgements

We acknowledge the financial support from MEITY (Grant No. 1
5(9)/2012-NANO(VOL-II)) for carrying out part of this work. N. 2
Srekanth acknowledges the postdoctoral fellowship from 3
SERB-NPDF (PDF/2016/002763), India. RKB acknowledges the 4
Marie-Sklodowska-Curie individual fellowship under EU H2020 5
Programme (H2020-IF-2017; Grant No: 750929). D. E.-L 6
and N. V. R. thank the EPSRC for support through funding for 7
the Centre for Doctoral Training in Fuel Cells and their Fuels 8
(EP/G037116/1, EP/L015749/1). A. J. P. thanks the EPSRC for 9
support through funding for the School of Physics and 10
Astronomy (EP/N509590/1). Central Instruments Facility, I.I.T. 11
Guwahati is acknowledged for providing the Raman, TEM, and 12
FESEM facilities. We thank Prof. M. Fujii, Kobe University, 13

Japan for help in the XPS measurement. We are thankful to Prof. M. Qureshi, Anindya S. Patra, Gaurangi Gogoi and Tushar Kanta Sahu for their help in PEC experiments.

References

- 1 C. G. Morales-Guio, L.-A. Stern and X. Hu, *Chem. Soc. Rev.*, 2014, **43**, 6555–6569.
- 2 H. Li, Y. Zhou, W. Tu, J. Ye and Z. Zou, *Adv. Funct. Mater.*, 2015, **25**, 998–1013.
- 3 Y. Lu, X. Cheng, G. Tian, H. Zhao, L. He, J. Hu, S.-M. Wu, Y. Dong, G.-G. Chang, S. Lenaerts, S. Siffert, G. Van Tendeloo, Z.-F. Li, L.-L. Xu, X.-Y. Yang and B.-L. Su, *Nano Energy*, 2018, **47**, 8–17.
- 4 X. Y. Xu, X. F. Dong, Z. J. Bao, R. Wang, J. G. Hu and H. B. Zeng, *J. Mater. Chem. A*, 2017, **5**, 22654–22661.
- 5 W. Zhou, W. Li, J.-Q. Wang, Y. Qu, Y. Yang, Y. Xie, K. Zhang, L. Wang, H. Fu and D. Zhao, *J. Am. Chem. Soc.*, 2014, **136**, 9280–9283.
- 6 W. Zhou, F. Sun, K. Pan, G. Tian, B. Jiang, Z. Ren, C. Tian and H. Fu, *Adv. Funct. Mater.*, 2011, **21**, 1922–1930.
- 7 Y.-P. Yuan, L.-W. Ruan, J. Barber, S. C. Joachim Loo and C. Xue, *Energy Environ. Sci.*, 2014, **7**, 3934–3951.
- 8 Y. Gai, J. Li, S.-S. Li, J.-B. Xia and S.-H. Wei, *Phys. Rev. Lett.*, 2009, **102**, 036402.
- 9 W. J. Zhou, Y. H. Leng, D. M. Hou, H. D. Li, L. G. Li, G. Q. Li, H. Liu and S. W. Chen, *Nanoscale*, 2014, **6**, 4698.
- 10 W. Zhou and H. Fu, *ChemCatChem*, 2013, **5**, 885–894.
- 11 K. K. Paul, S. Jana and P. K. Giri, *Part. Part. Syst. Charact.*, 2018, **35**, 1800198.
- 12 K. K. Paul, R. Ghosh and P. K. Giri, *Nanotechnology*, 2016, **27**, 315703.
- 13 K. K. Paul and P. K. Giri, in *Reference Module in Chemistry, Molecular Sciences and Chemical Engineering*, Elsevier, 2017, DOI: 10.1016/B978-0-12-409547-2.13176-2.
- 14 K. K. Paul and P. K. Giri, *J. Phys. Chem. C*, 2017, **121**, 20016–20030.
- 15 M.-Z. Ge, C.-Y. Cao, S.-H. Li, Y.-X. Tang, L.-N. Wang, N. Qi, J.-Y. Huang, K.-Q. Zhang, S. S. Al-Deyab and Y.-K. Lai, *Nanoscale*, 2016, **8**, 5226–5234.
- 16 A. Tanaka, A. Ogino, M. Iwaki, K. Hashimoto, A. Ohnuma, F. Amano, B. Ohtani and H. Kominami, *Langmuir*, 2012, **28**, 13105.
- 17 M. A. Khan, L. Sinatra, M. Oufi, O. M. Bakr and H. Idriss, *Catal. Lett.*, 2017, **147**, 811–820.
- 18 K. K. Paul and P. K. Giri, *J. Nanosci. Nanotechnol.*, 2019, **19**, 307–331.
- 19 F.-X. Xiao, S.-F. Hung, H. B. Tao, J. Miao, H. B. Yang and B. Liu, *Nanoscale*, 2014, **6**, 14950–14961.
- 20 J. Greeley, T. F. Jaramillo, J. Bonde, I. Chorkendorff and J. K. Nørskov, *Nat. Mater.*, 2006, **5**, 909.
- 21 S. Stankovich, D. A. Dikin, G. H. B. Dommett, K. M. Kohlhaas, E. J. Zimney, E. A. Stach, R. D. Piner, S. T. Nguyen and R. S. Ruoff, *Nature*, 2006, **442**, 282–286.
- 22 D. Escalera-López, Y. Niu, S. J. Park, M. Isaacs, K. Wilson, R. E. Palmer and N. V. Rees, *Appl. Catal., B*, 2018, **235**, 84–91.
- 23 C. Liu, L. Wang, Y. Tang, S. Luo, Y. Liu, S. Zhang, Y. Zeng and Y. Xu, *Appl. Catal., B*, 2015, **164**, 1–9.
- 24 Y. Dong, S.-Y. Chen, Y. Lu, Y.-X. Xiao, J. Hu, S.-M. Wu, Z. Deng, G. Tian, G.-G. Chang, J. Li, S. Lenaerts, C. Janiak, X.-Y. Yang and B.-L. Su, *Chem.-Asian J.*, 2018, **13**, 1609–1615.
- 25 Y. Kim, D. H. K. Jackson, D. Lee, M. Choi, T.-W. Kim, S.-Y. Jeong, H.-J. Chae, H. W. Kim, N. Park, H. Chang, T. F. Kuech and H. J. Kim, *Adv. Funct. Mater.*, 2017, **27**, 1701825.
- 26 B. Chen, E. Liu, T. Cao, F. He, C. Shi, C. He, L. Ma, Q. Li, J. Li and N. Zhao, *Nano Energy*, 2017, **33**, 247–256.
- 27 Y. Pi, Z. Li, D. Xu, J. Liu, Y. Li, F. Zhang, G. Zhang, W. Peng and X. Fan, *ACS Sustainable Chem. Eng.*, 2017, **5**, 5175–5182.
- 28 H. Li, Y. Wang, G. Chen, Y. Sang, H. Jiang, J. He, X. Li and H. Liu, *Nanoscale*, 2016, **8**, 6101–6109.
- 29 Y. Li, Y.-L. Li, C. M. Araujo, W. Luo and R. Ahuja, *Catal. Sci. Technol.*, 2013, **3**, 2214–2220.
- 30 D. Wang, Z. Wang, C. Wang, P. Zhou, Z. Wu and Z. Liu, *Electrochem. Commun.*, 2013, **34**, 219–222.
- 31 K. Y., H. Li, C. Li, Z. Tang, B. Guo, L. Xiang, H. Fu and Z. Zhu, *Sci. Rep.*, 2015, **5**, 18730.
- 32 D. Voiry, M. Salehi, R. Silva, T. Fujita, M. Chen, T. Asefa, V. B. Shenoy, G. Eda and M. Chhowalla, *Nano Lett.*, 2013, **13**, 6222–6227.
- 33 M. A. Lukowski, A. S. Daniel, F. Meng, A. Forticaux, L. Li and S. Jin, *J. Am. Chem. Soc.*, 2013, **135**, 10274–10277.
- 34 J. Xie, H. Zhang, S. Li, R. Wang, X. Sun, M. Zhou, J. Zhou, X. W. Lou and Y. Xie, *Adv. Mater.*, 2013, **25**, 5807–5813.
- 35 D. Escalera-López, Y. Niu, J. Yin, K. Cooke, N. V. Rees and R. E. Palmer, *ACS Catal.*, 2016, **6**, 6008–6017.
- 36 H. Li, C. Tsai, A. L. Koh, L. Cai, A. W. Contryman, A. H. Fragapane, J. Zhao, H. S. Han, H. C. Manoharan, F. Abild-Pedersen, J. K. Nørskov and X. Zheng, *Nat. Mater.*, 2015, **15**, 48.
- 37 J. Xie, H. Zhang, S. Li, R. Wang, X. Sun, M. Zhou, J. Zhou, X. W. Lou and Y. Xie, *Adv. Mater.*, 2013, **25**, 5807–5813.
- 38 W. Zhou, Z. Yin, Y. Du, X. Huang, Z. Zeng, Z. Fan, H. Liu, J. Wang and H. Zhang, *Small*, 2013, **9**, 140–147.
- 39 H. Yu, X. Yu, Y. Chen, S. Zhang, P. Gao and C. Li, *Nanoscale*, 2015, **7**, 8731–8738.
- 40 N. Zhang, S. Gan, T. Wu, W. Ma, D. Han and L. Niu, *ACS Appl. Mater. Interfaces*, 2015, **7**, 12193–12202.
- 41 X. Chia, N. A. A. Sutrisnroh and M. Pumera, *ACS Appl. Mater. Interfaces*, 2018, **10**, 8702–8711.
- 42 C. E. Blackmore, N. V. Rees and R. E. Palmer, *Phys. Chem. Chem. Phys.*, 2015, **17**, 28005–28009.
- 43 E. Kemppainen, A. Bodin, B. Sebok, T. Pedersen, B. Seger, B. Mei, D. Bae, P. C. K. Vesborg, J. Halme, O. Hansen, P. D. Lund and I. Chorkendorff, *Energy Environ. Sci.*, 2015, **8**, 2991–2999.
- 44 S. Li, T. Pu, J. Wang, X. Fang, Y. Liu, S. Kang and L. Cui, *Int. J. Hydrogen Energy*, 2018, **43**, 16534–16542.
- 45 K. K. Paul, N. Sreekanth, R. K. Biroju, T. N. Narayanan and P. K. Giri, *Sol. Energy Mater. Sol. Cells*, 2018, **185**, 364–374.
- 46 X.-Y. Yang, L.-H. Chen, Y. Li, J. C. Rooke, C. Sanchez and B.-L. Su, *Chem. Soc. Rev.*, 2017, **46**, 481–558.
- 47 N. Li, X. Zhang, W. Zhou, Z. Liu, G. Xie, Y. Wang and Y. Du, *Inorg. Chem. Front.*, 2014, **1**, 521–525.

- 1 48 S.-H. Nam, T. K. Kim and J.-H. Boo, *Catal. Today*, 2012, **185**, 259–262.
- 49 Z. Yin, Z. Zeng, J. Liu, Q. He, P. Chen and H. Zhang, *Small*, 2013, **9**, 727–731.
- 5 50 K. C. J. Lee, Y.-H. Chen, H.-Y. Lin, C.-C. Cheng, P.-Y. Chen, T.-Y. Wu, M.-H. Shih, K.-H. Wei, L.-J. Li and C.-W. Chang, *Sci. Rep.*, 2015, **5**, 16374.
- 51 D. Kiriya, M. Tosun, P. Zhao, J. S. Kang and A. Javey, *J. Am. Chem. Soc.*, 2014, **136**, 7853–7856.
- 10 52 A. Shaista, S. Arun Kumar and E. Jonghwa, *Sci. Technol. Adv. Mater.*, 2015, **16**, 035009.
- 53 B. Yue, Y. Ma, H. Tao, L. Yu, G. Jian, X. Wang, X. Wang, Y. Lu and Z. Hu, *J. Mater. Chem.*, 2008, **18**, 1747–1750.
- 15 54 K. Yang, J. Li, Y. Peng and J. Lin, *Phys. Chem. Chem. Phys.*, 2017, **19**, 251–257.
- 55 L. R. L. Ting, Y. Deng, L. Ma, Y.-J. Zhang, A. A. Peterson and B. S. Yeo, *ACS Catal.*, 2016, **6**, 861–867.
- 56 B. Santara, P. K. Giri, K. Imakita and M. Fujii, *Nanoscale*, 2013, **5**, 5476.
- 20 57 W. Ho, J. C. Yu, J. Lin, J. Yu and P. Li, *Langmuir*, 2004, **20**, 5865–5869.
- 58 M. Cueto, M. Piedrahita, C. Caro, B. Martínez-Haya, M. Sanz, M. Oujja and M. Castillejo, *J. Phys. Chem. C*, 2014, **118**, 11432–11439.
- 25 59 S.-M. Wu, X.-L. Liu, X.-L. Lian, G. Tian, C. Janiak, Y.-X. Zhang, Y. Lu, H.-Z. Yu, J. Hu, H. Wei, H. Zhao, G.-G. Chang, G. Tendeloo, L.-Y. Wang, X.-Y. Yang and B.-L. Su, *Adv. Mater.*, 2018, **30**, 1802173.
- 60 D. Hou, W. Zhou, X. Liu, K. Zhou, J. Xie, G. Li and S. Chen, *Electrochim. Acta*, 2015, **166**, 26–31.
- 61 Y. Li, H. Wang, L. Xie, Y. Liang, G. Hong and H. Dai, *J. Am. Chem. Soc.*, 2011, **133**, 7296–7299.
- 5 62 B. Ma, P.-Y. Guan, Q.-Y. Li, M. Zhang and S.-Q. Zang, *ACS Appl. Mater. Interfaces*, 2016, **8**, 26794–26800.
- 63 L. Liao, J. Zhu, X. Bian, L. Zhu, M. D. Scanlon, H. H. Girault and B. Liu, *Adv. Funct. Mater.*, 2013, **23**, 5326–5333.
- 64 R. K. Biroju, S. Pal, R. Sharma, P. K. Giri and T. N. Narayanan, *Nanotechnology*, 2017, **28**, 085101.
- 10 65 Y. Deng, L. R. L. Ting, P. H. L. Neo, Y.-J. Zhang, A. A. Peterson and B. S. Yeo, *ACS Catal.*, 2016, **6**, 7790–7798.
- 66 H. Nan, Z. Wang, W. Wang, Z. Liang, Y. Lu, Q. Chen, D. He, P. Tan, F. Miao, X. Wang, J. Wang and Z. Ni, *ACS Nano*, 2014, **8**, 5738–5745.
- 15 67 L. P. L. Mawlong, K. K. Paul and P. K. Giri, *J. Phys. Chem. C*, 2018, **122**, 15017–15025.
- 68 J. Deng, H. Li, J. Xiao, Y. Tu, D. Deng, H. Yang, H. Tian, J. Li, P. Ren and X. Bao, *Energy Environ. Sci.*, 2015, **8**, 1594–1601.
- 20 69 J. Hong, Z. Hu, M. Probert, K. Li, D. Lv, X. Yang, L. Gu, N. Mao, Q. Feng, L. Xie, J. Zhang, D. Wu, Z. Zhang, C. Jin, W. Ji, X. Zhang, J. Yuan and Z. Zhang, *Nat. Commun.*, 2015, **6**, 6293.
- 25 70 H. Li, C. Tsai, A. L. Koh, L. Cai, A. W. Contryman, A. H. Fragapane, J. Zhao, H. S. Han, H. C. Manoharan, F. Abild-Pedersen, J. K. Nørskov and X. Zheng, *Nat. Mater.*, 2015, **15**, 48.
- 30 71 X. Song, G. Chen, L. Guan, H. Zhang and J. Tao, *Appl. Phys. Express*, 2016, **9**, 095801.